Magnetic fabrics reveal three-dimensional flow processes within elongate magma fingers at the margin of the Shonkin Sag laccolith (MT, USA)

Jonas Köpping[1*], Alexander R. Cruden[1], Craig Magee[2], William McCarthy[3], John Geissman[4,5], Daniel Holm[6]

[1]*School of Earth, Atmosphere and Environment, Monash University, Melbourne, 3800, Australia*

[2] *School of Earth and Environment, University of Leeds, Leeds, LS2 9JT, UK*

[3]*School of Earth and Environmental Sciences, University of St. Andrews, UK*

[4] *Department of Geosciences, University of Texas at Dallas, Richardson, TX 75080, USA*

[5] *Department of Earth and Planetary Sciences, University of New Mexico, Albuquerque, NM 87131, USA*

[6] *Department of Earth Sciences, Kent State University, Kent, Ohio 44242, USA*

[*]Corresponding author: Jonas Köpping, jonas.koepping@erdw-ethz.ch

Author twitter handles: @JonasKoepping @SandyCruden @DrCraigMagee

This manuscript is a pre-print which has been accepted for publication in *Journal of Structural Geology* (https://doi.org/10.1016/j.jsg.2023.104829).

Accepted for publication in Journal of Structural Geology doi.org/10.1016/j.jsg.2023.104829

Magnetic fabrics reveal three-dimensional flow processes within elongate magma fingers at the margin of the Shonkin Sag laccolith (MT, USA)

Jonas Köpping[1*], Alexander R. Cruden[1], Craig Magee[2], William McCarthy[3], John Geissman[4,5], Daniel Holm[6]

[1]*School of Earth, Atmosphere and Environment, Monash University, Melbourne, 3800, Australia*

[2] *School of Earth and Environment, University of Leeds, Leeds, LS2 9JT, UK*

[3]*School of Earth and Environmental Sciences, University of St. Andrews, UK*

[4] *Department of Geosciences, University of Texas at Dallas, Richardson, TX 75080, USA*

[5] *Department of Earth and Planetary Sciences, University of New Mexico, Albuquerque, NM 87131, USA*

[6] *Department of Earth Sciences, Kent State University, Kent, Ohio 44242, USA*

[*]Corresponding author: Jonas Köpping, jonas.koepping@erdw-ethz.ch

Abstract

Unravelling magma flow in ancient sheet intrusions is critical to understanding how magma pathways develop and feed volcanic eruptions. Analyzing the shape preferred orientation of minerals in intrusive rocks can provide information on magma flow, because crystals may align parallel to the primary flow direction. Anisotropy of magnetic susceptibility (AMS) is an established method to quantify such shape preferred orientations in igneous sheet intrusions with weak or cryptic fabrics. However, use of AMS to characterize how magma flows within the individual building blocks of sheet intrusions (i.e., magma fingers and segments), hereafter referred to as elements, has received much less attention. Here we use a high spatial resolution sampling strategy to quantify the AMS of the Eocene Shonkin Sag laccolith (Montana, USA) and associated elongate magma fingers. Our results suggest that magnetic fabrics across the main

laccolith reflect sub-horizontal magma flow, and inferred flow directions suggest an underlying NE-SW striking feeder dyke. We interpret systematic changes in magnetic fabric shape and orientation across the magma fingers to reflect the interaction between competing forces occurring during along-finger magma flow (i.e., simple shear) and horizontal and vertical inflation (i.e., pure shear flattening). Local crossflow of magma between coalesced fingers increases the complexity of magma flow kinematics and related fabrics. Despite these complexities, the AMS in coalesced magma fingers maintain their internal flow- and inflation-related fabrics, which suggests that magma flow within the fingers remains channelized after coalescence. Given that many sheet intrusions consist of amalgamated elements, our findings highlight the need to carefully consider element distribution and sample locations when interpreting magma flow from AMS measurements.

1. Introduction

Magma transport in the Earth's upper crust is facilitated by networks of interconnected sheet intrusions (i.e., sills and dykes) (e.g., Anderson, 1937, 1951; Elliot and Fleming, 2004; Leat, 2008; Muirhead et al., 2012; Magee et al., 2016a; Schofield et al., 2017; Eide et al., 2021). These sills and dykes commonly form via the coalescence of discrete, laterally restricted elements, such as magma fingers and segments (Fig. 1; e.g., Pollard et al., 1975; Rickwood, 1990; Horsman et al., 2005; Schofield et al., 2012b; Galland et al., 2019; Magee et al., 2019; Stephens et al., 2021; Köpping et al., 2022): magma fingers have pipe-like geometries with large thickness-to-width ratios of ~0.1–1 and rounded intrusion tips, whereas segments have blade-like geometries with relatively small thickness-to-width ratios of ~<0.1 and sharp intrusion tips (see Magee et al., 2019 and references therein). Both magma fingers and segments are elongated parallel to their propagation direction, such that their long axes are a proxy for the primary magma flow direction (e.g., Pollard et al., 1975; Schofield et al., 2012b; Galland et al., 2019).

Previous studies of sheet intrusion elements have focused on their 3-D geometry and the host rock deformation mechanisms that accommodate their emplacement and growth (e.g., Pollard et al., 1975; Schofield et al., 2012a; Spacapan et al., 2017; Stephens et al., 2021; Köpping et al., 2022).

However, few studies have examined how the formation and coalescence of elements impacts internal magma flow kinematics (Horsman et al., 2005; Magee et al., 2013, 2016b). Yet deciphering how magma flows within elements, and whether it mixes or remains channelized when elements coalesce, is critical to understanding: (1) the formation and architecture of both sheet intrusions and upper-crustal magma plumbing systems (e.g., Muirhead et al., 2012; Magee et al., 2016a; Schofield et al., 2017); (2) the subsurface distribution of magma and its impact on potential eruption locations and volcanic hazards (e.g., Sparks, 2003; Cashman and Sparks, 2013); and (3) the formation of many Ni-Cu-PGE sulfide deposits, which commonly accumulate in areas of high magma flux within restricted magma channels such as elongate intrusions (e.g., tubular chonoliths) (e.g., Barnes et al., 2016).

[Insert Figure 1 here.]

Reconstructing magma flow in sheet intrusions is often accomplished using anisotropy of magnetic susceptibility (AMS) analyses, which are widely used for quantifying the average magnetic fabric of a rock sample (e.g., Knight and Walker, 1988; Tarling and Hrouda, 1993; Philpotts and Asher, 1994; Cruden et al., 1999; Ferré et al., 2002; Tauxe, 2003; Poland et al., 2004; Horsman et al., 2005; Morgan et al., 2008; McCarthy et al., 2015; Andersson et al., 2016; Magee et al., 2016b; Martin et al., 2019). These analyses are reliant on the preservation of magma flow patterns by the orientation of crystals during emplacement (e.g., Knight and Walker, 1988). Yet magnetic fabrics and their equivalent petrofabrics can be modified and overprinted by syn- and post-emplacement tectonic deformation, and by changing internal flow and crystallization processes (e.g., during element coalescence), which may complicate how they are interpreted (e.g., Riller et al., 1996; Andersson et al., 2016; Mattsson et al., 2018; Burchardt et al., 2019; Burton-Johnson et al., 2019; Martin et al., 2019). Furthermore, because parts of an intrusion (e.g., an element) may solidify and lock in fabrics with different orientations at different times during emplacement, it is likely that a range of processes, from initial propagation to inflation and potential late-stage backflow, will be recorded by fabrics within an intrusion (e.g., Philpotts and Philpotts, 2007). Given this potential variation in fabric orientation, a key limitation in previous magma flow studies, particularly of tabular intrusions, is that because sample locations are commonly widely distributed along the intrusion plane, they may record different and unrelated processes. High-resolution sampling strategies are therefore necessary to unravel the flow history of sheet intrusions in cross-sectional

outcrops (e.g., Cañón-Tapia and Herrero-Bervera, 2009; Magee et al., 2013, 2016b; Andersson et al., 2016; Morgan et al., 2017; Martin et al., 2019). Although some AMS studies with high-resolution sampling strategies have been conducted in sheet intrusions that likely comprise coalesced elements, the internal flow kinematics within elongate pipe-like elements remain uncertain (Magee et al., 2016b; Hoyer and Watkeys, 2017; Martin et al., 2019). There are likely two competing emplacement mechanisms that will control the orientation and shape of fabrics in elements: (1) alignment of crystals broadly parallel to the magma flow, defined by an axially symmetric, parabolic velocity profile, assuming laminar Poiseuille flow (e.g., Leite, 1959; Knight and Walker, 1988) (Figs. 2A–2B); and (2) flattening of fabrics against the walls during magma finger inflation (e.g., Merle, 2000) (Fig. 2B). Initial fabrics are likely to be flow related but may be modified and overprinted by pure shear flattening strain during intrusion growth (e.g., Merle, 2000). It is important to note that fabrics recorded in AMS data reflect the strain at the time of local magma solidification during magma emplacement. Therefore, the effect of each individual emplacement mechanism on both fabric orientation and shape as well as the amount of fabric overprinting may vary between individual sample locations.

[Insert Figure 2 here.]

Here, we present AMS and petrofabric data from both the main Shonkin Sag laccolith, Montana, USA (e.g., Weed and Pirsson, 1895; Pirsson, 1905; Osborne and Roberts, 1931; Barksdale, 1937; Hurlbut Jr, 1939; Kendrick and Edmond, 1981; Ruggles et al., 2021), and discrete and coalesced, well-exposed elongate magma fingers that emerge from the laccolith's southeast margin (Fig. 3) (Pollard et al., 1975). The southeast margin exposure represents an ideal study location because the magma fingers have a well-defined long axis, equivalent to the primary magma flow direction, and are easily accessed for high-resolution sampling (Pollard et al., 1975). By combining AMS and petrofabric analyses of samples collected from the Shonkin Sag laccolith and its marginal magma fingers, this study aims to investigate: (1) potential emplacement and flow kinematics of the Shonkin Sag laccolith; (2) whether magnetic fabrics in both discrete and coalesced magma fingers reflect primary magma flow; (3) if flow in two coalesced fingers was sheet-like (i.e., magma mixed) and the coalesced fingers behaved as one body, or if flow remained localized within individual fingers; and (4) any potential differences and similarities between magnetic fabrics within the Shonkin Sag laccolith and its marginal magma fingers.

A combination of regional mapping (Montana Bureau of Mines and Geology, 2021) and magnetic fabric analyses suggests that the Shonkin Sag laccolith was fed by an underlying NE-SW striking dyke and that fabrics recorded within both discrete and coalesced magma fingers reflect an interplay of finger-parallel magma flow and horizontal and vertical inflation. Local crossflow of magma may occur where fingers coalesce; however, fabrics observed in most areas of coalesced magma fingers maintain their internal flow- and inflation-related fabrics, which suggests that magma flow within the fingers remains channelized after coalescence. Understanding where magma flow channelizes in igneous sheet intrusions provides a better understanding of internal magma transport and intrusion growth processes, which is important for improving knowledge on the architecture of both sheet intrusions and trans-crustal magma plumbing systems. Channelized magma flow further locally increases the magma flux, which enhances the potential for thermal-mechanical erosion of surrounding host rocks and subsequent incorporation of host rock xenoliths into the magma (e.g., Barnes et al., 2016). This process contributes to making space for the intruding magma and increases its crustal sulfur content, leading to the formation of economically significant Ni-Cu-PGE deposits (e.g., Uitkomst Complex) (e.g., Gauert et al., 1996; Barnes et al., 2016). Identifying areas of channelized magma flow within sheet intrusions therefore has implications for Ni-Cu-PGE exploration.

2. Geological setting

Cenozoic felsic and mafic igneous intrusive and volcanic rocks of the Highwood Mountains are part of the Central Montana alkalic province (Figs. 3A–3B) (Weed and Pirsson, 1895; Pirsson, 1905; Barksdale, 1937; Hurlbut Jr, 1939; Buie, 1941; Burgess, 1941; Pollard et al., 1975; Kendrick and Edmond, 1981; Henderson et al., 2012). The early Eocene (~52 ± 1 Ma) formation of the Highwood Mountains occurred in two stages: (1) volcanic eruptions, which emplaced both quartz latite flows and silicic pyroclastic rocks; and (2) later volcanism with mafic phonolite flows (e.g., Hurlbut Jr, 1939; Burgess, 1941; Larsen, 1941; O'Brien et al., 1991). Mafic igneous intrusions linked to the second stage of volcanism include a radial dyke swarm surrounding the main volcanic complex, as well as sills, laccoliths, and chonoliths that have a range of magma compositions (e.g., shonkinite, syenite, biotite pyroxenite) (Figs. 3B–3C) (e.g., Hurlbut Jr, 1939; Buie, 1941; Burgess,

1941; Larsen, 1941; Nash and Wilkinson, 1970, 1971; O'Brien et al., 1991; Henderson et al., 2012).

[Insert Figure 3 here.]

The samples used in this study were collected from the Shonkin Sag laccolith, a ~51 Ma old, ~70 m thick, sub-circular sheet intrusion with a diameter of ~2.3–3 km (Fig. 3B) (e.g., Barksdale, 1937; Marvin et al., 1980). Five sills (No 1–5) emerge from the southeast margin of the laccolith; at a distance of >266 m from the laccolith edge, three of these sills split into elongate magma fingers (Fig. 3D) (Pollard et al., 1975). The main Shonkin Sag laccolith is characterized by layering of shonkinite and syenite. This layering has been the subject of a number of petrologic studies for over a century, with debate focusing on whether the igneous layering formed by differentiation of a single magma pulse or by injection of multiple magma pulses (e.g., Pirsson, 1905; Osborne and Roberts, 1931; Barksdale, 1937; Hurlbut Jr, 1939; Kendrick and Edmond, 1981; Ruggles et al., 2021). Based on magnetic fabric measurements, structural analysis and thermal modelling, Ruggles et al. (2021) suggest that the Shonkin Sag laccolith was emplaced via at least seven discrete magma pulses over a period of ca. 3 years, while subsequent differentiation and solidification of the laccolith may have occurred over ca. 21 years. Most of the laccolith and all of the igneous sills that emerge from its southeast margin are made of porphyritic shonkinite with clinopyroxene, olivine, and (pseudo)leucite phenocrysts hosted in a fine-to-medium grained groundmass of biotite, clinopyroxene, and olivine (e.g., Pirsson, 1905; Osborne and Roberts, 1931; Barksdale, 1937; Hurlbut Jr, 1939; Nash and Wilkinson, 1970; Kendrick and Edmond, 1981; Henderson et al., 2012; Ruggles et al., 2021). Ruggles et al. (2021) identified magnetite as the dominant magnetic mineral associated with magnetic fabrics at the margin of the laccolith and within the sills. Here we focus on magnetic fabrics and petrofabrics within elongate, SE trending magma fingers, which emerge from the sills located at the SE laccolith margin (Fig. 3D) (Pollard et al., 1975). These fingers are of meter-scale with thickness-to-width ratios of 0.1–0.83 and they crop out in a large main cliff face, and in multiple blocks detached from the cliff (Fig. 3D, Supplemental Material S0) (Pollard et al., 1975). The detached blocks remain upright and have not been transported far, so we can map individual magma fingers across them to study the 3D finger geometry (Pollard et al., 1975).

3. Methods and background

3.1. Sample location and preparation

Samples were collected from twenty-three locations at varying elevation levels across the Shonkin Sag laccolith and from twenty-one locations within two discrete and two coalesced magma fingers at the SE laccolith margin (sample locations are given in Supplemental Material S1). Based on their clustered spatial location, samples collected from the interior of the laccolith were divided into four groups, located NNE, W, SW, and S of the geographic laccolith center (referred to as SSL-1, SSL-2, SSL-3, and SSL-4, respectively). The two coalesced magma fingers, named Hb and Hc, and the discrete magma fingers, named II and JJ, emerge from sill No. 5 and are located ~305 m and ~500 m east of the laccolith-sill-transition, respectively (Fig. 3D). Samples collected from magma fingers are labeled by the finger ID and a continuous number (e.g., II-1, II-2, II-3, etc…). In order to use magnetic fabrics and petrofabrics to assess potential magma flow kinematics within the magma fingers, we collected oriented sample cores from: (1) the finger centers; (2) close to the top and bottom finger margins; and (3) close to the lateral tips of each magma finger. For the two coalesced fingers Hb and Hc, additional samples were collected from the step that connects the vertically offset fingers. Samples were collected away from the quenched, mm- to cm-thick, highly-fractured, glassy margin that surrounds many of the magma fingers. All collected samples were cut into ~2.2 cm long cylinders resulting in 262 specimens and an average of eleven specimens per sample location across the main laccolith, and 127 specimens and an average of six specimens per sample location within the magma fingers.

3.2. Magnetic fabric analyses

The AMS fabrics of specimens collected from the interior of the Shonkin Sag laccolith were measured using an AGICO KLY-3S Kappabridge at the University of New Mexico, with a magnetic field of 423 m/A and a frequency of 875 Hz. Specimens collected from the magma fingers were analyzed using an AGICO KLY5 Kappabridge with an attached 3-D-rotator in the M^3Ore Lab at the University of St. Andrews. Analyses were conducted using a magnetic field of 400 m/A and a frequency of 1220 Hz.

The magnetic susceptibility (K) of each analyzed specimen is described by a second-rank tensor, which is commonly visualized as a magnitude ellipsoid with the principal eigenvectors, or susceptibilities, K_1, K_2, and K_3 being the maximum, intermediate, and minimum axes of the ellipsoid, respectively (e.g., Khan, 1962; Hrouda, 1982). Where AMS ellipsoids have a prolate shape ($K_1 > K_2 \simeq K_3$), K_1 may be interpreted to represent the magma flow or stretching direction, whereas oblate fabrics ($K_1 \simeq K_2 > K_3$) may represent the magma flow or stretching/imbrication plane (K_1-K_2 plane) (e.g., Knight and Walker, 1988; Cruden and Launeau, 1994). Notably, for imbricated fabrics, the imbrication closure has been interpreted to point in the direction of magma transport (Fig. 2A) (e.g., Knight and Walker, 1988; Philpotts and Philpotts, 2007). The mean, or bulk, susceptibility (K_m) of an AMS ellipsoid is defined as:

$$K_m = \frac{K_1 + K_2 + K_3}{3} \quad (1)$$

and is measured in SI units. Additional parameters that describe the AMS ellipsoid include the dimensionless corrected anisotropy degree (P_j) and the shape parameter (T) (Jelinek, 1981). The corrected anisotropy degree is:

$$P_j = exp\sqrt{2[\,(\eta_1 - \eta_m)^2 + (\eta_2 - \eta_m)^2 + (\eta_3 - \eta_m)^2\,]}, \quad (2)$$

where $\eta_m = \frac{\eta_1+\eta_2+\eta_3}{3}$, $\eta_1 = \ln(K_1)$, $\eta_2 = \ln(K_2)$, and $\eta_3 = \ln(K_3)$. P_j ranges from 1–2, whereby 1 is an isotropic ellipsoid (i.e., a sphere), and $P_j > 1$ indicating the percentage anisotropy, such that $P_j = 1.3$ describes an ellipsoid with 30% anisotropy. The AMS ellipsoid shape is quantified by:

$$T = \frac{2\eta_2 - \eta_1 - \eta_3}{\eta_1 - \eta_3}, \quad (3)$$

whereby T = 1 describes a uniaxial oblate shape (i.e., planar magnetic fabric) and T = –1 describes a uniaxial prolate shape (i.e., linear magnetic fabric). Fabrics presented in this study are classified as weakly (0 – -0.33), moderately (-0.34 – -0.66), and strongly (-0.67 – -1) prolate, or as weakly

(0–0.33), moderately (0.34–0.66), and strongly (0.67–1) oblate. The scalar AMS ellipsoid parameters (i.e., K_m, P_j, T) and magnitude and orientation of the principal susceptibilities (K_1, K_2, K_3) were calculated using Anisoft5 (v. 5.1.03; AGICO 2019). The geographically corrected orientations of K_1, K_2, and K_3 for each sample location were plotted on equal-area, lower hemisphere stereographic projections (a.k.a. stereonets) and the orientations of the mean principal susceptibilities and their 95% confidence ellipses were calculated using a tensor averaging routine (Jelinek, 1981). Magnetic foliation and lineation measurements are classified as gently (0–30º), moderately (31–60º), and steeply (61–90º) dipping or plunging, respectively. To identify the link between magnetic fabrics and the magma finger geometry, we also quantified the angles between the magma finger long axis measured in the field and both the magnetic foliation strike (α) and the lineation (β), respectively (Fig. 2C).

After describing the magnetic fabrics, we characterize the AMS of the samples into two groups of distinct fabrics that either have a gentle to sub-horizontal magnetic foliation (*Fabric Type 1*) or a steep to sub-vertical magnetic foliation (*Fabric Type 2*). *Fabric Type 2* is further subdivided into four groups based on fabric orientation and magnetic ellipsoid shape. We use this classification to discuss a potential link between individual fabrics as well as a potential fabric deformation history during the emplacement of elongate elements.

3.3. Magnetic mineralogy

During magma flow, crystals can develop a shape-alignment that is parallel to the magma flow direction due to a combination of progressive pure and simple shear, such that the petrofabric foliation and lineation indicate the magma flow plane and axis, respectively (Fig. 2A) (e.g., Ildefonse et al., 1992; Launeau and Cruden, 1998; Horsman et al., 2005). Crystals may also become aligned and imbricated due to strong velocity gradients that can occur in magma at intrusion margins, such that the closure of the resulting imbricated foliation planes points in the direction of magma flow (Figs. 2A–2B) (e.g., Knight and Walker, 1988; Cañón-Tapia and Chávez-Álvarez, 2004; Poland et al., 2004; Philpotts and Philpotts, 2007). Pure shear flattening due to intrusion inflation and propagation may also result in a foliation that is parallel to the closest host rock contact (Figs. 2A–2B). Importantly, AMS fabrics can be affected by mineralogical controls

on the dominating magnetic phases, increasing the complexity in linking these fabrics to magma flow processes.

The magnetic fabric of ferrimagnetic (s.l.) minerals (e.g., magnetite, maghemite) is influenced by their grain size, shape anisotropy, domain state, and/or grain distribution (Hrouda, 1982; Potter and Stephenson, 1988; Tarling and Hrouda, 1993; Dunlop and Özdemir, 2001; Ferré, 2002). Previous combined petrofabric and magnetic fabric studies have shown that the distribution and shape of magnetite grains are commonly controlled by a framework of the volumetrically dominant silicate mineral phases (e.g., Cruden and Launeau, 1994; Launeau and Cruden, 1998; O'Driscoll et al., 2008). For example, in grains that are large enough to include multiple magnetic domains, referred to as a multi-domain (MD) state, the minimum and maximum magnetic susceptibility coincide with the short- and long-dimension of the grains, respectively, and the magnetic lineation coincides with the SPO (Dunlop and Özdemir, 2001).

Although silicate and magnetic fabrics often correlate, there are instances where they differ (e.g., Launeau and Cruden, 1998; Rochette et al., 1999; Mattsson et al., 2021). For example, where the magnetic fabric is carried by small single-domain (SD) grains, the minimum and maximum magnetic susceptibilities are parallel to the long- and short-dimension of the grain, respectively (Hrouda, 1982; Potter and Stephenson, 1988; Dunlop and Özdemir, 2001; Ferré, 2002). This "inversion" (an inverse fabric) is caused by a higher susceptibility to magnetization along the easy magnetization axis, which is perpendicular to the long-dimension of SD grains (Hrouda, 1982; Potter and Stephenson, 1988; Dunlop and Özdemir, 2001). Magnetic rock fabrics that are purely formed by MD or SD magnetite therefore result in *normal* or *inverse* fabrics, respectively. In such cases, normal fabrics coincide with the magnetite petrofabric, and inverse fabrics form perpendicular to the magnetite petrofabric, where K_1 is perpendicular to the petrofabric foliation and K_3 is parallel to the lineation (Potter and Stephenson, 1988; Rochette and Fillion, 1988; Rochette et al., 1999; Ferré, 2002). Magnetic fabrics that cannot be classified as *normal* or *inverse* are termed *intermediate* and may form when the AMS is carried by a combination of MD and SD magnetite grains (Rochette et al., 1999; Ferré, 2002). Alternatively, where clusters of closely spaced magnetite grains form within a silicate framework, the magnetic responses of multiple grains may magnetically interact (Hargraves et al., 1991; Mattsson et al., 2021). In this case, the shape preferred orientation (SPO) of magnetite plays a secondary role and the AMS is dominated

by the grain distribution (distribution anisotropy), which may result in non-coaxial silicate petrofabrics and the magnetic fabrics (Stacey, 1960; Hargraves et al., 1991; Mattsson et al., 2021).

The formation of normal, inverse, or intermediate magnetic fabrics and the potential occurrence of a distribution anisotropy make the interpretation of AMS data challenging. It is therefore important to understand the magnetic carriers and their controls on the AMS fabric. To determine the magnetic mineralogy of our samples, we measured the thermomagnetic properties of one specimen from a sample from one of the magma fingers collected in this study, and six specimens from samples collected at sites established through a complete vertical transect in the center of the laccolith (SSL-4). We also obtained isothermal remanent magnetization (IRM) acquisition and backfield isothermal remanent magnetization (BIRM) data on thirteen specimens. Finally, we carried out three-component thermal demagnetization of anhysteretic remanent magnetization (ARM) in a fashion similar to that described by Lowrie (1990) for three component thermal demagnetization of IRM; these analyses were conducted for six specimens collected at two sample locations along a single traverse through the Shonkin Sag laccolith (Supplemental Material S2). Measurements were carried out at the M^3Ore Lab, University of St. Andrews and in the laboratory at the University of Texas at Dallas. For our analyses, samples that may reflect inverse or intermediate fabrics and samples with a low-to-high bulk susceptibility were selected to get a representative range of mineralogy of the samples studied. The low-to-high temperature, low-field-susceptibility experiments were conducted by measuring the bulk magnetic susceptibility of a powdered rock specimen using a CS4 and CS-L heating and cooling attachment for the KLY-5 Kappabridge. The specimen was first cooled down to -194 ºC and the bulk susceptibility was recorded during heating to room temperature and then up to 700 ºC, before the temperature was reduced back to room temperature. This procedure provides susceptibility data from a continuous heating-cooling cycle from -194 ºC to 700 ºC. For specimens collected within the Shonkin Sag laccolith, susceptibility data was collected during a continuous heating-cooling cycle from room temperature to 700 ºC. The arising data were collected and used to determine the Verwey transition and the Curie temperature to identify the main ferrimagnetic (s.l.) phase (Dunlop and Özdemir, 2001). Isothermal remanent magnetization acquisition experiments were conducted by using the following procedure: (1) whole core specimens were demagnetized using an LDA5 AF Demagnetizer in an alternating maximum field of 200 mT, and a medium decrease rate; (2) the demagnetized specimens were inserted into a MMPM10 pulse magnetizer and exposed to a set

field along a single axis direction; (3) the remanence of each sample was then measured in a JR6 spinner magnetometer; (4) steps 2 and 3 were repeated as the IRM field was progressively increased from 0.015 T to 1 T. BIRM measurements were subsequently performed by: (1) placing the same specimen upside down in the MMPM10 pulse magnetizer; (2) applying an IRM and then measuring the samples remanence in the JR6 magnetometer; (3) steps 1 and 2 were repeated until the magnetic remanence stopped decreasing and started to increase, usually around 0.1 T.

Petrography inspection of thin sections prepared from representative specimens of the magma fingers was evaluated using a polarizing transmitted and reflected light microscope to determine the textural relationship between oxide and silicate mineral phases. Additional μm-scale images of the thin sections were collected with a scanning electron microscope (Quanta 600 MLA), operated with an acceleration voltage of 20 kV, and the chemical composition of these specimens was determined using energy dispersive X-ray analysis.

3.4. Quantification of petrofabrics using high-resolution 3-D X-ray computed tomography

The petrofabric of silicate phases (i.e., pyroxene and olivine) in seven selected magma finger specimens was quantified using high-resolution, 3-D X-ray computed tomography (HRXRCT) images. We selected one specimen at each sample location of Finger Hc (Hbc6, Hc7–Hc11) to create a complete HRXRCT dataset for one magma finger, as well as one specimen at JJ-2, which produces tight 95% confidence ellipses and AMS axes orientations that may reflect primary magma flow. HRXRCT data were collected to test if silicate petrofabrics reflect the magnetic fabrics, which aids in identifying the physical significance of the AMS and in better understanding the interplay between AMS and petrofabrics. Samples were scanned using a Zeiss Versa XRM520 3-D X-ray microscope at the Australian Resources Research Centre (CSIRO Mineral Resources, Perth, Australia). Scans were conducted using a flat panel detector and an acceleration voltage of 120 kV and 10 W. A total of 1,601 projections of the stepwise rotating sample were recorded, which were then merged and stitched to create a 3-D volumetric grid with a voxel size of ~12 μm. We post-processed these grids in Avizo 2020.1 (ThermoFischer) to reduce noise and to separate individual phases, as per Godel (2013). We applied an edge preserving non-local mean filter and

manually separated silicate mineral phases from the groundmass based on their grayscale intensity values. Where grayscale intensity values of silicate phases and the groundmass overlap, we calculated variance volumes that were then used to separate the individual mineral phases. Avizo internal functions such as 'Remove islands' and 'Fill holes' were applied to the separated objects to reduce noise. Both pyroxene and olivine phenocrysts within the shonkinite samples analyzed are ~1–10 mm in size and are clearly visible in hand specimens (Fig. 4A). We therefore classify small, separated objects with a volume <1 mm^3 as noise and extracted the long, intermediate, and short axis orientations of silicate mineral phases with volumes above this threshold value. The resulting geographic orientations of the mineral phase long and short axes are visualized in equal-area, lower hemisphere stereonets as orientation density distribution contours (modified Kamb method with exponential smoothing (Vollmer, 1995); mplstereonet Python package v.0.6.2). The average SPO is described by a fabric tensor with $V_1 > V_2 > V_3$ representing the long, intermediate, and short axis of the corresponding best fit ellipsoid, respectively, weighted by the axis length (Petri et al., 2020; Mattsson et al., 2021). We analyzed the fabric tensor of each sample using the TomoFab Matlab toolbox (v.1.3) (Petri et al., 2020).

We used the same HRXRCT workflow to separate oxide grains within the same specimens. Object volumes < 10^6 μm^3 were removed to limit noise effects. To identify a potential influence of the spatial distribution of oxide phases on the magnetic fabric, we calculated the distribution anisotropy (DA) tensor for oxides using the TomoFab Matlab toolbox (v.1.3) as per Mattsson *et al.* (2021). The DA tensor is defined by the DA eigenvectors $\lambda_1 > \lambda_2 > \lambda_3$ representing the long, intermediate, and short axis of the DA ellipsoid, respectively. Relatively low values of the corrected degree of anisotropy (P_j) indicate a random grain distribution, whereas relatively high P_j values indicate that grains are spatially distributed along planes ($T > 0$) or lines ($T < 0$) (Mattsson et al., 2021).

4. Results

Here we present: (1) petrographic descriptions of shonkinite samples; (2) results of the rock magnetic experiments; and (3) field observations and magnetic- and petro-fabrics measured in samples collected from the main Shonkin Sag laccolith and the four magma fingers. Orientation

measurements are given as strike/dip and trend/plunge for planar and linear features, respectively. Average petrofabric and magnetic fabric measurements of sample sites are presented in Table 1 and 2, respectively; measurements of individual specimens are presented in the Supplemental Material S3 and S4.

4.1. Petrography

The magma fingers are entirely porphyritic shonkinite with a medium-grained groundmass of clinopyroxene, olivine, leucite, minor biotite, and opaque oxides such as magnetite (Fig. 4). Phenocrysts of clinopyroxene, olivine, and leucite are of mm-to-cm size, visible in hand specimens, and float in the groundmass (Figs. 4A–4B). HRXRCT measurements indicate 25–35 vol. % of phenocrysts and 65–75 vol. % groundmass (Supplemental Material S5). Up to ~1 cm long, euhedral clinopyroxene phenocrysts have a shape preferred orientation, and locally form star-shaped clusters (Figs. 4A–4D; cf. Hurlbut 1939). Olivine phenocrysts are of mm size, have a euhedral shape, and are occasionally zoned (Fig. 4E). Leucite phenocrysts are euhedral and their diameter ranges from < 1 mm up to ~4 mm (Fig. 4F). Magnetite was identified in both reflected-light and scanning-electron microscopy as the dominant oxide phase (Figs. 4G–4I). Magnetite grains are commonly unaltered and are widely distributed in the shonkinite groundmass, and reflect an interstitial phase (Fig. 4G–4H). Clusters of magnetite were not identified in petrographic analyses, which is supported by a relatively low degree of distribution anisotropy (P_j = 1.034–1.241; Table 1). The petrography of the magma fingers is similar to the main Shonkin Sag laccolith documented in numerous studies (e.g., Pirsson, 1905; Barksdale, 1937; Hurlbut Jr, 1939; Nash and Wilkinson, 1970; Ruggles et al., 2021).

[Insert Figure 4 here.]

4.2. Magnetic mineralogy

The results of rock magnetic experiments permit a further determination of the principal magnetic phase that carries the AMS. A low-to-high temperature, low-field-susceptibility experiment determined the Verwey transition and Curie point for sample Hc9 (Fig. 5A). The measurements show a steep initial increase in K_m between -197 ºC and the Verwey transition at -165 ºC followed

by a decrease to 5.6 ºC, after which K_m values increase slowly to a well-defined peak at a temperature of about 483 ºC, which is followed by a rapid decrease in K_m as temperatures increase to > 600 °C (Fig. 5A). The well-defined Curie point is at about 570 ºC (Fig. 5A). During cooling, the K_m measurements show a steep increase between 600 ºC and 358 ºC followed by a moderate decrease to 48 ºC (Fig. 5A). The measurements collected within the Shonkin Sag laccolith (SS-62–SS-66, SS-69) show a well-defined K_m peak at a temperature between ~520–535 ºC, followed by a rapid decrease in K_m as temperatures increase to > 600 ºC (Fig. 5B). The Curie point occurs at about 580 Cº and 605 ºC for samples SS-62–SS-66 and SS-69, respectively (Fig. 5B). During cooling, K_m values steeply increase between about 580 ºC and 490 ºC followed by a gentle increase to ~430 ºC and a moderate decrease to ~50 ºC (Fig 5B). A second peak is observed at lower temperatures during both heating (~ 310 ºC) and cooling (~370 ºC) for SS-69 (Fig. 5B).

[Insert Figure 5 here.]

IRM and BIRM measurements are useful for characterizing magnetic mineralogy and to estimate magnetic grain size (Dunlop and Özdemir, 2001). IRM experiments show a rapid increase in remanence over a range of low inducing fields and 95% of saturation is achieved by 48 to 78 mT for most of the thirteen specimens analyzed (Fig. 6). The saturation isothermal magnetization (SIRM) for these specimens always is reached below 210 mT with no significant variation observed above this threshold. By extrapolating BIRM curves, we determined the coercivity of remanence (H_{CR}) which ranges from 10 to 15 mT (Fig. 6). Three specimens (Hb1, Hb3, JJ-4) have a higher coercivity. The IRM curves of these specimens rapidly increase within low inducing fields, however, 95% of saturation is reached by 97, 87, and 200 mT, respectively (Figs. 6A, 6C). SIRM occurs below 210 mT for Hb1 and Hb3, and by 1000 mT for JJ-4. H_{CR} measurements based on extrapolated BIRM curves for these samples indicate relatively high coercivity of remanence values of 22 to 29 mT (Fig. 6).

[Insert Figure 6 here.]

4.3. AMS and petrofabric analyses

Here we describe: (1) magnetic fabrics of samples collected from the interior of the Shonkin Sag laccolith; and (2) field observations, magnetic fabrics, and petrofabrics of samples collected from

magma fingers at the SE laccolith margin. Samples from the main laccolith are presented in merged groups based on their spatial sample location. Magnetic- and petro-fabrics observed within magma fingers are described with respect to the nearest intrusion contact at each individual magma finger.

[Insert Table 1 and Table 2 here.]

4.3.1. Shonkin Sag laccolith

Magnetic fabrics were analyzed in four sample groups located to the north-northeast, west, southwest, and south of the geographic center of the Shonkin Sag laccolith (SSL-1, SSL-2, SSL-3, and SSL-4; Fig. 7A). All groups have similar bulk magnetic susceptibilities (K_m) and corrected degree of anisotropy (P_j) values, and their AMS ellipsoids are of similar shape (T) (Table 1). K_m of individual specimens ranges from 0.565 x 10^{-2}–11.12 x 10^{-2} SI, with an average of 3.43 x 10^{-2} SI (Fig. 7B). The specimens have relatively low P_j values, which increase slightly from 1.0038 to 1.0732 with increasing K_m (Fig. 7B). AMS ellipsoids of specimens have moderately prolate to strongly oblate shapes (T = -0.65–0.97) (Fig. 7C).

The magnetic foliation of rocks collected in all sample groups is sub-horizontal and parallel to the inferred upper and lower contacts of the laccolith. Magnetic lineations in SSL-1 are shallow and oriented NE-SW (229/07º), and this trend approximately coincides with the overall trend of dykes (069º NE) that crop out NE of the Highwood Mountains (Fig. 7C; indicated by red lines in the stereonets). Magnetic lineations for SSL-2 (173/04º) and both SSL-3 (309/01º) and SSL-4 (314/02º) are oriented N-S and NW-SE, respectively, at a high angle (~75º) to the aforementioned NE-SW trending dykes (Fig. 7C). We note that the K_1 and K_2 axes of specimens in SSL-1, SSL-2, and, to a minor extent also in SSL-4, are scattered, which causes the 95% confidence ellipses to locally overlap (Fig. 7C). The scattered K_1 axis orientations are grouped in two individual clusters in SSL-2 and SSL-4, trending NNW and WNW, and ENE and NW, respectively (Fig. 7C).

[Insert Figure 7 here.]

4.3.2. Magma fingers

For the two individual magma fingers (i.e., Finger II and Finger JJ) and coalesced magma fingers Hb-Hc we describe field observations, AMS data, and, where available, petrographic analysis of

fabrics. We describe rock fabrics based on their location with respect to the nearby intrusion contact. Samples are subsequently characterized into two groups of distinct fabrics that either have a gentle to sub-horizontal foliation (*Fabric Type 1*) or a steep to sub-vertical foliation (*Fabric Type 2*).

Most specimens of the magma fingers have high magnetic K_m values on the order of 10^{-2} SI and only one (JJ-4) out of twenty-one samples has specimens with lower K_m values of ~10^{-4} SI (Table 2). The corrected degree of anisotropy (P_j) values of individual specimens range from 1.010 to 1.030 (Table 2). In most specimens (JJ-2, Hbc6, and Hbc8–Hbc11), the silicate petrofabric foliation is approximately parallel to the corresponding magnetic foliation.

4.3.2.1. Finger II

Finger II is approximately 1.75 m wide and 0.3 m thick, with upper and lower contacts concordant with bedding in the Eagle Sandstone formation (114/01º NE and 121/02º NE, respectively; Fig. 8A). The lateral tips of Finger II are blunt to rectangular, and the exposed part of the eastern contact is oriented 145/80º SW (Fig. 8A). Host rock deformation in the vicinity of the lateral tips cannot be determined due to erosion and scree cover (Fig. 8A). P_j values of samples collected at Finger II range from 1.018–1.030 and K_m varies between 3.03 x 10^{-2} SI and 4.10 x 10^{-2} SI (Table 2).

Samples located 3–4 cm from the upper and lower intrusion contact are characterized by a steep to moderate magnetic foliation (II-2 = 175/74º W; II-4 = 163/49º ENE), a gently to moderately NNW plunging magnetic lineation (II-2 = 342/39º; II-4 = 350/09º), and a weakly to moderately prolate fabric shape (T = -0.49 – -0.31) (Fig. 8, Table 2). At these locations, the magnetic foliations form a moderate to steep angle of 47.5–74.5º to the nearby sub-horizontal host rock contacts, and strike at an α angle of up to 30º to the magma finger long axis, which trends 145º SE (Figs. 8B). In contrast to samples near the upper and lower finger contacts, measured magnetic foliations located 2–6 cm from the lateral finger tips (II-1 = 145/89º NE; II-5 = 153/60 º SW) strike at an α angle of 0–8º to the magma finger long axis and are thus sub-parallel to the intrusion contact (Fig. 8B). Samples II-1 and II-5 are characterized by a steeply and gently plunging magnetic lineation (II-1 = 142/72º; II-5 = 316/28º), and a moderately oblate (T = 0.35) and weakly prolate (T = -0.16)

fabric shape, respectively. In the intrusion core (i.e., II-3), approximately 15–16 cm to the upper and lower intrusion contacts and 37 cm to the eastward lateral finger tip, the magnetic foliation (022/84º E) is steeply dipping and strikes at an α angle of 57º to the magma finger long axis. The mean K_1 orientation of II-3 is steep (157/81º), orthogonal to the upper and lower contacts, and the fabric shape is weakly oblate (T=0.20).

[Insert Figure 8 here.]

4.3.2.2. Finger JJ

Finger JJ is approximately 2.1 m wide and 0.45 m thick and has strata-concordant flat top and bottom contacts (138/03º NE and 126/02º NE, respectively; Fig. 9A). The lateral tips of Finger JJ are asymmetric, being pointed to the SW and blunt on the NE where it is oriented 135/80º NE (Fig. 9A). Host rock bedding at the lateral tips of Finger JJ is deflected upwards (Fig. 9A). P_j values of samples collected at Finger JJ range from 1.011–1.027 and K_m varies between 0.04 x 10^{-2} SI and 4.30 x 10^{-2} SI with K_m at JJ-4 being two orders of magnitude smaller than the remaining samples (Table 2).

The magnetic foliations of samples located 3–6 cm from the upper and lower intrusion contact (JJ-2 = 086/04º N; JJ-4 = 086/05º S) are sub-parallel to the nearby intrusion contact (138/03º NE, 126/02º NE), and the shallow plunging K_1 (327/03º, 117/03º) trends approximately parallel to the magma finger long axis (135º SE). In both JJ-2 and JJ-4, the mean principal susceptibility directions are well-defined and have tight 95% confidence ellipses (Fig. 9B). The fabric shape at JJ-2 is weakly prolate (T = -0.06), whereas JJ-4 has a moderately oblate shape (T = 0.39). In contrast, sample JJ-5 is located ~9 cm from the NE lateral finger tip and is characterized by a steep magnetic foliation (131/83º SW), which is sub-parallel to the intrusion contact (135/80º NE). The magnetic lineation at JJ-5 is steeply plunging (248/83º) and the fabric shape is weakly oblate (T = 0.13). Individual specimen K_1, K_2, and K_3 directions in sample JJ-5 are slightly dispersed but 95% confidence ellipses are tight (Fig. 9B). Samples JJ-1 and JJ-3 are located 18–27 cm from the upper and lower intrusion contacts and are considered to represent the intrusion core. JJ-1 is located ~31 cm from the SW lateral finger tip and has a steep magnetic foliation (030/75º SE) that strikes sub-

perpendicular to the magma finger long dimension (135º SE) (Fig. 9B). The mean K_1 axis is gently plunging SW (207/12º) and the fabric shape is weakly prolate (T = -0.11). In contrast to JJ-1, JJ-3 is characterized by a steep magnetic foliation (135/73º NE) and a gently plunging lineation (133/05º) that strikes and plunges sub-parallel to the magma finger long dimension, respectively (Fig. 9B). The fabric shape at JJ-3 is weakly prolate (T = -0.21).

Petrofabric analyses of silicate phases at JJ-2 indicate a sub-horizontal foliation (026/06º SE) sub-parallel to the nearby host rock contact, which coincides with the magnetic foliation. In contrast to the SE trending mean K_1 axis (327/03º), V_1 gently plunges ENE (073/04º) at an angle of 62º to the magma finger long dimension (Fig. 9C; Table 1). The petrofabric shape is moderately oblate (T = 0.38), which contrasts with the weakly prolate magnetic counterpart (Tables 1–2).

[Insert Figure 9 here.]

4.3.2.3. Coalesced Fingers Hb-Hc

Coalesced magma fingers Hb and Hc are approximately 6.7 m and 1.9 m wide, 1.2 m and at least 0.7 m thick, respectively, with sub-horizontal, strata-concordant upper and lower contacts (104/02º NNE, 079/01º NNW, 108/02º NNE; Fig. 10A). The NE lateral tip of Finger Hc has a blunt to rectangular geometry and forms a steeply dipping (118/72º SW) crosscutting contact with the host rock (Fig. 10A). Host rock deformation at the lateral tip remains undefined due to erosion. The upper contacts of Fingers Hb and Hc are vertically offset with Finger Hb being ~0.65 m higher than the top contact of Hc. A ~0.75 m wide and ~0.4 m thick, NE-dipping step connects Fingers Hb and Hc, and it has a gently dipping (143/18º NE), strata-discordant upper contact with host rock bedding (Fig. 10A). P_j values of samples collected at Fingers Hb and Hc range from 1.010–1.025 and K_m varies between 2.10 x 10^{-2} SI and 3.87 x 10^{-2} SI (Table 2).

Three samples are located close to the upper or lower intrusion contacts (Hb1=15 cm, Hb3=20 cm, Hc7=8 cm). Hb1 and Hb3 are characterized by gently inclined magnetic foliations, which are at an angle of 30º and 27º with the respective nearby contact, and by gently plunging lineations (Hb1 = 050/20º; Hb3 = 251/18º) (Fig. 10B). The magnetic foliations of the weakly oblate Hb1 (013/30º ESE; T = 0.08) and the moderately prolate Hb3 (117/25º SW; T = -0.41) dip toward and away

from the adjacent intrusive step to the east, respectively (Fig. 10B). The NE-SW trend of K_1 in both Hb1 (050/20º) and Hb3 (251/18º) points toward the adjacent WNW-ESE striking intrusive step with a high β angle of 47–68º to the magma finger long axis (118º SE) (Fig. 10B, Table 2). In contrast to Hb1 and Hb3, Hc7 has a moderately dipping magnetic foliation (145/63º SW) at an angle of ~63º to the nearby contact. The magnetic lineation (211/60º) plunges SW and the fabric shape at Hc7 is moderately oblate (T=0.44).

Samples Hbc5 and Hbc6 are located 13 cm and 20 cm from the upper intrusion contact, within the intrusive step that connects the fingers Hb and Hc, and they have weakly prolate (T=-0.15) and moderately oblate (T=0.41) fabric shapes, respectively (Fig. 10A). At both locations, the magnetic foliation is moderately and steeply dipping (Hbc5 = 031/58º SE, Hbc6 = 082/71º S) and K_1 axes orientations are moderately and steeply plunging south (Hbc5 = 162/51º, Hbc6 = 194/70º). The magnetic foliation at Hbc5 forms an angle of 53º to the nearby host rock contact; contact orientation measurements above Hbc6 cannot be determined due to limited 3D exposure (Fig. 10A).

Sample Hc8 was collected 17 cm from the lateral SW finger tip of Hc and has a weakly oblate fabric shape (T=0.03) (Fig. 10A). Hc8 is characterized by a steeply dipping magnetic foliation (030/84º SE) at an angle of 86º to the nearby contact (118/72º SW), and a steeply plunging K_1 axes orientations (194/70º) (Fig. 10A–B).

Samples Hb2, Hb4, and Hc9–Hc11 are located in the core of the intrusions with distances of ~30–50 cm to the closest upper or lower intrusion contact (Fig. 10A) and are characterized by a steep to sub-vertical magnetic foliation. Except for Hb4, magnetic foliations within the intrusion core are striking SW (Hb2 = 143/73º NE, Hc9 = 128/80º NE, Hc10 = 157/79º NE, Hc11 = 116/87º NE) with alpha angles of 2–39º to the finger long axis orientation (Fig. 10B). K_1 axis orientations at Hb2 are moderately plunging SE (129/37º), whereas at Hc9–Hc11, K_1 axes are steep to sub-vertical (Hc9 = 019/79º, Hc10 = 013/71º, Hc11 = 345/86º; Table 2). The ellipsoid shape of the described fabrics ranges from weakly to moderately prolate at Hb2, Hc10, and Hc11, and is weakly oblate at Hc9 (Table 2). The magnetic foliation (034/86º NE) and lineation (261/85º) at Hb4 dip and plunge sub-vertical, and they are both oriented sub-perpendicular to the magma finger long dimension (118º) (Fig. 10B). The fabric shape at Hb4 is weakly oblate (T=0.05).

[Insert Figure 10 here.]

Petrofabric analyses of the main silicate phases (i.e., pyroxene and olivine) at Hbc6 and Hc7–Hc11 indicate a moderately to strongly oblate fabric shape (T = 0.38–0.78) except for Hc11, which is weakly prolate (T = -0.10). The petrofabric foliation at Hbc6, Hc8, Hc9, and Hc11 approximately reproduces the magnetic foliation, with angles between both foliation planes ranging from 11º to 34º (Fig. 11A–B). Except for Hc8 where foliations are oriented approximately perpendicular to the magma finger long dimension (118º), petrofabric and magnetic foliations at Hbc6, Hc9, and Hc11 strike SE, approximately in the magma finger long dimension. At Hc10, both petrofabric and magnetic foliations dip NE. However, the gently dipping petrofabric foliation (127/32º NE) contrasts with the steep magnetic foliation (157/79º NE), which form at an angle of 52º (Fig. 11B). A comparable deviation in foliation orientations is observed at Hc7 (Fig. 11B). Here, the petrofabric foliation is shallowly dipping north (084/22º N), whereas the magnetic foliation is moderately dipping SW (145/63º SW), resulting in an angle of 75º between both foliation planes. In all analyzed specimens, the mean V_1 axes orientations are sub-horizontal to gently plunging, which contrasts with the steep to sub-vertical K_1 axes orientations (Fig. 11B).

[Insert Figure 11 here.]

4.3.3. Characterization of fabric types

Four samples collected in the magma fingers (JJ-2, JJ-4, Hb1, Hb3) and all four sample groups collected within the main laccolith (SSL-1 – SSL-4) are characterized by sub-horizontal to gently inclined magnetic foliations and lineations, which we refer to as *Fabric Type 1*. Within the magma fingers, *Fabric Type 1* is only observed in samples collected within 3–19 cm of the upper and lower margins of Fingers JJ and Hb (Figs. 9, 10; Table 2). We note that although samples <8 cm from the upper and lower margins were collected from Finger II (II-2, II-4) and Hc (Hc-7), they do not display the characteristics of *Fabric Type 1* (Figs. 8 and 10).

In contrast to the sub-horizontal *Fabric Type 1*, *Fabric Type 2* is characterized by moderate to sub-vertical magnetic foliations, which are further subdivided into four distinct groups based on their orientation and shape. Five samples (II-2, II-4, II-5, JJ-3, Hb2) are characterized by a steep to

moderate magnetic foliation approximately striking parallel to the magma finger long dimension, a gently to moderately plunging magnetic lineation, and a weakly to moderately prolate fabric shape (T = -0.49 – -0.16), which we refer to as *Fabric Type 2A* (Figs. 8–10; Table 2). Similar to *Fabric Type 2A*, the magnetic foliation of *Fabric Type 2B* (II-1, JJ-5, Hbc6, Hc7, Hc9) strikes approximately parallel to the magma finger long dimension. The magnetic lineations, however, are steep to sub-vertical and fabric shapes are weakly to moderately oblate (T = 0.13–0.44). Two samples (Hc10, Hc11) have a steep to sub-vertical magnetic foliation and lineation and weakly prolate shapes (T = -0.31 – -0.25), which we characterize as *Fabric Type 2C* (Figs. 10B–10C). The magnetic foliation at these locations strikes oblique to sub-parallel to the magma finger long dimension (α = 2º–39º). *Fabric Type 2D* is characterized by a moderately inclined (Hbc5) and steep to sub-vertical (II-3, JJ-1, Hb4, Hc8) magnetic foliations that strike sub-perpendicular to the magma finger long axis (Figs. 8B, 9B, 10B). The magnetic lineation at these locations plunges steeply (II-3, Hb4, Hc8), moderately (Hbc5), and gently (JJ-1) and the fabric shape ranges from weakly prolate to weakly oblate (T = -0.15 – 0.20).

5. Discussion

5.1. Characterization of the magnetic mineralogy and the significance of AMS

5.1.1. Magnetic mineralogy

Based on rock magnetic experiments and petrographic observations, Ruggles et al. (2021) suggested that both magnetite and titanomagnetite with a pseudo-single domain (PSD) state and multidomain (MD) state are the dominant magnetic phases in the rocks exposed at the margin of the Shonkin Sag laccolith and its peripheral sills. Our observations support the dominance of titanomagnetite as the magnetic carrier within the magma fingers based on: (1) a relatively high K_m of > ~10^{-2} SI (Tarling and Hrouda, 1993); (2) rapidly increasing K_m followed by a slightly temperature dependent flat plateau in low-temperature regimes between -197–5 Cº (Fig. 5A) (Dunlop and Özdemir, 2001); and (3) a Curie point estimate of 570 ºC (Fig. 5A) (Dunlop and Özdemir, 2001). The Curie Point of pure magnetite occurs at 580 ºC; however, this temperature decreases for titanomagnetite with increasing Ti content (Akimoto, 1962). The Curie point

estimate of 570 ºC suggests that titanomagnetite with a low Ti content of ~1–2 % is the dominant ferrimagnetic phase in the samples studied (Akimoto, 1962).

IRM and BIRM measurements also indicate that the AMS of all samples is dominated by a relatively low coercivity phase such as titanomagnetite. IRM curves and the magnetic field strength required to completely saturate a sample (SIRM) can be used to estimate the magnetic grain size (cf. Dunlop and Özdemir, 2001). MD magnetite will completely saturate by ~80–200 mT, fine grained SD magnetite will completely saturate by ~300 mT, and SIRM values just above ~200 mT indicate the presence of PSD grains (Dunlop and Özdemir, 2001). The relatively low SIRM of < 210 mT for twelve out of thirteen samples indicate a PSD to MD state (Fig. 6) (Dunlop and Özdemir, 2001). IRM and BIRM measurements combined with low-to-high temperature susceptibility data suggest that PSD to MD titanomagnetite are the dominant phases responsible for the AMS in the marginal sills and comprising magma fingers, and by comparison to related studies, the main Shonkin Sag laccolith (Ruggles et al., 2021). Samples with higher coercivities (Hb1, Hb3, JJ-4) are located near the upper or lower margin of magma fingers (Fig. 6). We suggest that weathering or alteration caused by interaction between the intruding magma and the pore water-saturated host rock may have altered titanomagnetite to relatively high coercivity minerals close to the host rock contact (Dunlop and Özdemir, 2001). Potential effects of these high coercivity minerals on the AMS fabrics have been considered during fabric interpretation.

5.1.2. Origin of the magnetic fabrics

Before interpreting primary magma flow and magma emplacement mechanisms from AMS data, it is important to first consider whether the magnetic fabrics measured have been affected and/or altered by other processes. Ruggles et al. (2021) found that MD and PSD magnetite are the dominant magnetic phases in shonkinite rocks at the margin of the laccolith, and where the rocks are undeformed and fresh they considered magnetic fabrics in their samples to be normal primary magma flow fabrics. However, a range of processes can modify and should be considered when interpreting magnetic fabrics. For example, magnetic foliation planes and/or magnetic lineations at a high-angle to the plane of a magma finger (i.e., *Fabric Type 2D*) (Figs. 8B, 9B, and 10B) may possibly be interpreted as intermediate or inverse fabrics due to the presence of SD magnetite

(Potter and Stephenson, 1988; Rochette and Fillion, 1988; Rochette et al., 1999). We can discount *Fabric Type 2D* being related to the presence of SD magnetite populations as our IRM analyses indicate no detectable SD magnetite, so we consider that sub-vertical magnetic lineations and foliations that strike sub-perpendicular to the magma finger long axis are unlikely to be caused by mineralogical affects. Alternatively, when magnetite grains are closely spaced or occur in clusters, adjacent grains can interact magnetically to alter magnetic fabrics (Hargraves et al., 1991; Mattsson et al., 2021). Because our petrographic analyses found no magnetite clusters, together with the generally low degree of distribution anisotropy (Table 1), distribution anisotropy of magnetite probably can be ruled out as contributing to the AMS of our samples.

Syn- and post-emplacement tectonic deformation can modify or completely overprint magma emplacement-related magnetic fabrics, which can add further complexity to the interpretation of AMS data. However, the Highwood Mountains of Montana are tectonically undeformed (e.g., Pollard et al., 1975), making it an ideal location to study magma emplacement processes and flow kinematics within intrusions. During tectonic overprinting, uniform fabrics representing the strain associated with tectonism should affect all sample locations (e.g., Burton-Johnson et al., 2019). Although uniform sub-horizontal magnetic foliations have been documented within the main Shonkin Sag laccolith (Fig. 7C), considerable variations in magnetic fabrics within the marginal magma fingers (Figs. 8B, 9B, 10B) are interpreted to indicate that no tectonic overprinting occurred. Alternatively, inverse magnetic fabrics can occur when they align with cooling joints oriented orthogonal to the intrusion margin (Trippanera et al., 2020). In this scenario, K1 axes will be oriented parallel to the fracture trend orthogonal to the intrusion margin due to potential secondary magma migration during relatively slow intrusion cooling (Trippanera et al., 2020). However, cooling joints in the magma fingers located at the SE margin of the Shonkin Sag laccolith are rare to absent, and magnetic fabrics within samples collected near minor fractures (e.g., II-2–II-4) are not parallel to the fracture plane. This suggests that magnetic fabrics in the Shonkin Sag magma fingers were not affected by fractures. Relatively rapid cooling rates should characterize the magma fingers due to their small size (0.3–1.2 m thick; 1.75–6.7 m wide), suggesting that convective magma flow is unlikely to have occurred within them (e.g., Gibb and Henderson, 1992; Holness et al., 2017). The lack of evidence for post-emplacement overprinting, cooling joints, or convective flow, together with the coincidence between the magnetic foliation strike and lineation trend with magma finger long axes in many samples (Figs. 8B, 9B, and 10B),

suggest that the AMS data from our samples can be interpreted to reflect primary syn-emplacement processes such as magma flow and/or intrusion inflation.

5.2. Shonkin Sag laccolith emplacement

Samples from sites established in all four arbitrary areas of the Shonkin Sag laccolith (SSL-1, SSL-2, SSL-3, SSL-4) yield a sub-horizontal magnetic foliation and a predominantly oblate fabric shape, regardless of their location (Fig. 7). These observations are consistent with measurements at the laccolith margin in areas of no to little deformation and/or alteration (Ruggles et al., 2021). The shape and orientation of magnetic fabrics observed across the Shonkin Sag laccolith may reflect sub-horizontal magma flow and/or vertical shortening, likely related to initial emplacement processes and, possibly, the subsequent inflation and/or deflation of the laccolith soon after emplacement. In primary magma flow within sheet-like intrusions, we expect the magnetic foliation to form parallel to the magma flow plane and K_1 principal axes will be aligned in the flow direction (Figs. 2A–2B) (e.g., Knight and Walker, 1988). The alignment of K_1 occurs due to progressive simple shear flow and results in monoclinic fabrics with plane strain ellipsoids ($T \approx 0$) (e.g., Cruden and Launeau, 1994; Ferré et al., 2002; Poland et al., 2004; Horsman et al., 2005). Alternatively, during vertical inflation of igneous sheet intrusions due to the continued throughput of magma, magnetic fabrics will record vertical shortening caused by progressive pure shear flattening strain, which results in biaxial, oblate fabrics ($T > 0$ to 1) (Fig. 2B) (e.g., Roni et al., 2014). During inflation the fabric shape at the intrusion margin will become progressively more oblate and the foliation will align with the orientation of the closest host rock contact (e.g., Roni et al., 2014).

[Insert Figure 12 here.]

We interpret sub-horizontal, oblate magnetic fabrics within the main Shonkin Sag laccolith to record a combination of sub-horizontal magma flow and vertical intrusion inflation. Assuming that K_1 indicates the primary magma flow direction, we suggest that the AMS within the laccolith indicates: (1) NE-SW oriented magma flow NNE of the intrusion center (SSL-1; K_1 = 229/07º); (2) NNW-SSE oriented magma flow W of the intrusion center (SSL-2; K_1 = 173/04º); and (3) NW-

SE oriented magma flow SW and S of the intrusion center (SSL-3 and SSL-4; K_1 = 309/01º and 314/02º, respectively) (Fig. 12). We note that samples across the main laccolith were collected from varying elevation levels (Supplemental Material S1), such that they may reflect fabrics within multiple magma pulses, which may explain both the slightly dispersed K_1 axis orientations and the formation of two K_1 axis clusters in sample groups SSL-2 and SSL-4 (Fig. 7C). The strongly oblate fabric shape across all four sample groups may reflect flattening of the fabrics against the roof, which is consistent with a conceptual model suggested by Morgan (2018), who applied Pascal's principle to explain laccolith emplacement. We interpret the maintenance of preferred K_1 axis orientations in sample groups SSL1–SSL4 to reflect primary magma flow during horizontal laccolith growth. Based on the data available, the relative timing of K_1 axis alignment parallel to the magma flow direction cannot be determined such that the alignment may have occurred both before and/or after laccolith inflation and resulting horizontal overburden uplift.

Feeders of sills and laccoliths are commonly described to be either linear, such as dykes and inclined sheets, or point-like conduits, from which magma flows linearly or radially, respectively (e.g., Cruden et al., 1999; Ferré et al., 2002; Galerne et al., 2011). If the Shonkin Sag laccolith was fed via a point source, we would expect the feeder to be located approximately in the intrusion center, which would be the origin of a radial magma flow pattern. However, this scenario is not supported by the NNW-SSE to NW-SE trending magnetic lineation at sample groups SSL-2, SSL-3, and SSL-4 (Fig. 12). We suggest that the Shonkin Sag laccolith was fed via a NE-SW striking dyke that terminated in the NE quadrant of the laccolith, close to sample group SSL-1 (Fig. 12). NW-SE directed flow of magma sub-perpendicular to the strike of the feeder is consistent with K_1 orientations in sample groups SSL-2, SSL-3, SSL-4 (Figs. 7C, 12). The NE-SW trending K_1 direction in sample group SSL-1 is sub-parallel to the strike of the potential feeder-dyke. We therefore hypothesize that the dyke terminated S to SW of sample group SSL-1, which may have resulted in a fanning magma flow pattern near the dyke tip (Fig. 12).

Although Pollard et al. (1975) assumed radial magma flow from the laccolith center to explain the NW-SE trend of magma fingers at the SE laccolith margin, similar magma finger trends are also consistent with magma being supplied via a NE-SW striking dyke (Fig. 12). In this scenario, linear magma flow sub-perpendicular to the feeder dyke coincides with the long-dimension of magma fingers (Fig. 12). Numerous NE-SW striking dykes are located SW of the laccolith, and they are

part of the radial dyke swarm that surrounds the main volcanic complex of the Highwood Mountains (Figs. 3B–3C). These observations suggest NE directed magma transport from the main volcanic complex toward the Shonkin Sag laccolith, which supports our proposed feeder model. Additional magnetic fabric analyses of samples from the eastern part of the laccolith could help to test the proposed model and to better constrain both the feeder type and location.

5.3. Tying magnetic fabrics to magma finger emplacement and growth

Given that we have determined that the magnetic fabrics likely record magma emplacement processes, we hypothesize there are two competing mechanisms that control the shape and orientation of fabrics in pipe-like intrusions, namely primary magma flow and intrusion inflation (Fig. 2B). For example, assuming primary magma flow along a horizontal magma finger, we expect crystals to align with the magma velocity profile, resulting in horizontal foliations close to the upper and lower contact and steep foliations near the lateral magma finger tips (e.g., Merle, 2000) (Figs. 2B, 13A). In both cases, the foliation parallels the nearest intrusion contact and K_1 aligns in magma finger long dimension, which we interpret to reflect the primary magma flow direction. Imbricated foliations may occur at distance to the upper and lower magma finger contacts due to the magma velocity gradient (e.g., Knight and Walker, 1988) (Figs. 2A–2B). During magma finger emplacement, magma fingers both increase in width and vertically inflate (e.g., Galland et al., 2019). This magma finger inflation causes pure shear flattening strain which may modify the initial, flow-related fabrics (e.g., Merle, 2000). For example, in case of vertical intrusion inflation, we expect foliations near the upper and lower intrusion margin to parallel the nearest contact with K_1 remaining aligned in finger long dimension, whereas at lateral finger tips, fabrics may become stretched along the intrusion contact, resulting in steep K_1 axes (Fig. 13A). During magma finger widening, we expect fabrics at the lateral magma finger tips to flatten against the nearest intrusion contact, likely resulting in steep foliations and lineations (Fig. 13A). Primary magma flow and intrusion inflation can occur simultaneously, producing a hybrid fabric that may be dominated by one process or the other. Importantly, AMS data reflect magnetic fabrics at the time of local magma solidification such that individual samples collected across the magma fingers

may reflect different emplacement stages (e.g., Philpotts and Philpotts, 2007). Spatially variable magma flow may therefore result in adjacent fabrics that are not directly related (Fig. 13A).

Below, we use magnetic fabric data, petrofabric analyses and field observations to interpret the emplacement of magma fingers located at the margin of the Shokin Sag laccolith. Critically, we interpret the primary magma finger flow direction to parallel the SE trend of the magma fingers, which point away from their feeding sills and the main Shonkin Sag laccolith (Pollard et al., 1975). This allows us to focus on interpreting internal 3-D flow within the elongate magma fingers, to tie magnetic fabrics to intrusion emplacement and growth, and test our hypothesis of competing emplacement mechanisms (i.e., primary magma flow and intrusion inflation) as outlined above.

[Insert Figure 13 here.]

5.3.1. Fabric Type 1 – Primary magma flow and vertical intrusion inflation

Fabric Type 1 is comparable to fabrics observed within the Shonkin Sag laccolith (Fig. 7C). As within the Shonkin Sag laccolith, we interpret *Fabric Type 1* to have formed during sub-horizontal magma flow and/or vertical shortening (Figs. 13A–13B). Because vertical magma finger inflation commonly occurs simultaneously with horizontal magma flow, we consider it likely that *Fabric Type 1,* as observed in the upper and lower magma finger margins (JJ-2, JJ-4, Hb1, Hb3), represents a hybrid of both processes, where the relative effect of each process may vary between locations (Fig. 13B). For example, the sub-horizontal foliation in samples JJ-2 and JJ-4 is sub-parallel to the closest upper or lower intrusion-host rock contact and K_1 trends sub-parallel to the finger long axis (Fig. 9B). In combination with the weakly prolate to moderately oblate fabric shape, these orientations suggest that progressive simple shear during magma flow may be the dominant process recorded by the AMS, superimposed by pure shear flattening due to minor vertical shortening (Fig. 13B). Considering the sample locations and assuming that magma solidification occurs first at the intrusion margins, we interpret the magnetic fabrics in samples JJ-2 and JJ-4 represent primary magma flow during a relatively early emplacement stage (Figs. 13A–13B).

A similar interpretation may account for the magnetic fabrics in samples Hb1 and Hb3 that are located close to the upper and lower margins of Finger Hb (Fig. 10A). In contrast to the sub-horizontal foliation in samples JJ-2 and JJ-4, the magnetic foliation in samples Hb1 and Hb3 dip gently in the direction of the magma finger long axis or away from the intrusive step that connects Fingers Hb and Hc (Fig. 10). These gently dipping foliations in rocks located close to the sub-horizontal intrusion-host rock contact, combined with their weakly oblate to moderately prolate AMS ellipsoids may indicate a relatively low degree of vertical flattening. We could also interpret the gently dipping foliations to be imbricated fabrics, whereby sample Hb1 records primary magma flow towards the SE and sample Hb3 indicates a foliation inclined toward either the former lateral tip of Finger Hb or to the intrusive step that connects Fingers Hb and Hc, potentially indicating crossflow between Hb and Hc (Figs. 10, 13A) (e.g., Magee et al., 2016b). Given the weakly oblate to moderately prolate AMS ellipsoids in these samples, we interpret K_1 to be a primary magma flow indicator. Therefore, their NE-SW trending K_1 directions may indicate flow oblique (β = 47º–68º) to the finger long axis, possibly related to local flow of magma between Fingers Hb and Hc after they had coalesced (Fig. 13A), or magma flow toward a solidified step. Because primary magma flow within sheet intrusions is commonly described to form oblate fabrics parallel to the flow plane with K_1 aligned in flow direction, similar to *Fabric 1*, we propose that *Fabric 1* could be the starting point for fabrics classified as *Fabric 2*, which we interpret below (Figs. 13B–13C). We note that fabrics close to the lateral magma finger tips may start as steep foliations instead of a *Fabric 1* due to combined simple and pure shear flow close to the steep intrusion contact (Figs. 13A–13B).

5.3.2. Fabric Type 2A, 2B – Horizontal shortening caused by intrusion widening

We interpret the moderate to steep magnetic foliations to represent magma emplacement processes because they strike slightly oblique to the magma finger long axis (α = 0–30º) and the magnetic lineation is gently to moderately plunging and broadly parallels the magma finger axis (Table 2). These fabrics are observed near to upper and lower intrusion contacts (II-2, II-4), at lateral finger tips (II-5), and along the centerline of magma fingers (JJ-3, Hb2). *Type 2A* fabrics may result from the superimposition of a sub-horizontal, oblate *Type 1* fabric, by a sub-horizontal NE-SW

shortening strain, approximately perpendicular to the magma finger long dimension (Figs. 13B–13C). Previous field studies have shown that space for magma fingers can be partly accommodated by host rock shortening when magma pushes against the host rock ahead of both the frontal and lateral intrusion tips (e.g., Pollard et al., 1975; Wilson et al., 2016; Spacapan et al., 2017; Galland et al., 2019). This process may result in compaction, folding, and shear failure of host rock layers and is commonly associated with blunt to rectangular intrusion tips as is observed in Fingers II and Hc (Figs. 8A, 10A) (Wilson et al., 2016; Spacapan et al., 2017; Galland et al., 2019; Stephens et al., 2021; Walker et al., 2021). We suggest that when magma fingers widen, magma or magma mush near the host rock walls gets squeezed, resulting in horizontal fabric shortening sub-perpendicular to the lateral margins and in vertical fabric stretching, which is reflected in the development of a new or overprinting fabric (i.e., Fabric Type 2B; Figs. 13B–13C). Similar modification of fabrics within an inflating finger could occur adjacent to an internal steeply inclined transient boundary, such as an inwardly migrating crystallization front (Fig. 13A). Regardless, this NE-SW shortening causes pure shear flattening of fabrics against lateral intrusion-host rock contacts or internal boundaries (II-5), resulting in steep foliations sub-parallel to the host rock contact (Figs. 13B–13C). We also hypothesize that the strength of fabric overprinting decays with distance from the lateral tip or internal boundary, which may for example be reflected by the more prolate AMS ellipsoid of II-2, II-4, JJ-3, and Hb2 compared to sample II-5 (Fig. 13B).

The magnetic foliation in *Fabric Type 2B* is slightly oblique to the magma finger long axis (α = 0–36º) and the samples that exhibit this fabric type are located close to (II-1, JJ-5) and farther away from (Hbc6, Hc7, Hc9) lateral finger tips, which suggests that they may record similar magma emplacement processes as described for *Fabric Type 2A* (i.e., horizontal NE-SW intrusion inflation). However, in contrast to *Fabric Type 2A* where K_1 plunges gently to moderately along the magma finger, K_1 of *Fabric Type 2B* is steeply inclined (Figs. 13B–13C; Table 2). As in *Fabric Type 2A*, horizontal intrusion inflation may have led to NE-SW pure shear flattening as well as fabric stretching at lateral intrusion tips, which resulted in the formation of *Type 2B* fabrics (Figs. 13B–13C). The weakly to moderately oblate AMS ellipsoids suggest a higher degree of NE-SW pure shear flattening compared to *Fabric Type 2A* (Fig. 13C). *Fabric Type 2B* may therefore reflect a more advanced stage of magma finger widening compared to *Fabric Type 2A*. The *Type 2B* fabric in sample Hbc6 is associated with the step that connects Fingers Hb and Hc. Here, the

magnetic foliation strikes E-W, which indicates potential local crossflow of magma between the coalesced magma fingers (Fig. 13A).

5.3.3. Fabric Type 2C, 2D – Horizontal shortening caused by intrusion lengthening

Similar AMS ellipsoid axes orientations in both *Type 2B* and *2C* fabrics suggest a formation of *Fabric Type 2C* due to the sequence of magma emplacement processes as described above (cf. *Fabric Type 2A* and *2B*) (Figs. 13B–13C). However, in contrast to the weakly to moderately oblate *Type 2B* fabrics, the AMS ellipsoid of *Fabric Type 2C* is weakly to moderately prolate with a steep to sub-vertical K_1 direction (Figs. 10, 13C). Assuming that *Fabric Type 2C* formed by progressive deformation of *Fabric Type 2B*, two scenarios may be considered: (1) vertical stretching during NE-SW magma finger widening (Figs. 13A–13B); or (2) horizontal NW-SE shortening at an arrested frontal finger tip due to continued magma supply (Figs. 13B–13C). When magma fingers widen and magma pushes against the host rock or against a transient solidification boundary (cf. *Fabric 2A*, *2B*), vertical flow along the boundary may result in stretching fabrics (Figs. 13A–13B). Field observations of clinopyroxene crystals oriented sub-parallel to the intrusion-host rock contact at lateral finger tips are consistent with this hypothesis (Fig. 2D). However, the effect of vertical stretching in samples Hc10 and Hc11 should be minor because they are located approximately in the core of Finger Hc. This is also reflected in the silicate mineral lineation, which plunges gently in the finger long axis direction, contrasting with the sub-vertical magnetic fabrics (Fig. 11B). Alternatively, sub-horizontal shortening parallel to the NW-SE finger long axis may have overprinted a sub-vertical, NW-SE striking, weakly to moderately oblate *Fabric Type 2B* foliation, resulting in steep, weakly prolate magnetic fabrics (Hc10, Hc11; Figs. 13B–13C). As noted above, NW-SE shortening is likely to occur at frontal magma finger tips (e.g., Cruden and Launeau, 1994; Magee et al., 2016b) and may also occur away from an arrested intrusion tip if magma supply continues (Figs. 13B–13C) (Cruden and Launeau, 1994).

With increasing horizontal shortening and pure shear flattening strain parallel to the magma finger long axis, *Type 2C* fabrics may evolve into steep to sub-vertical (II-3, JJ-1, Hb4, Hc8), or moderately inclined (Hbc5), weakly prolate to weakly oblate fabrics, which strike sub-perpendicular to the finger long axis (i.e., *Fabric Type 2D*; Figs. 13B–13C). Alternatively, a sub-

vertical foliation may form due to free grain rotation of minerals, which then become trapped with their long and intermediate SPO axes perpendicular to the flow direction (e.g., Cañón-Tapia and Chávez-Álvarez, 2004). If this rotation occurs within a crystallizing, horizontally flowing magma, the growing framework of silicate phases may prevent further rotation of grains toward the magma flow plane, resulting in sub-vertical magnetic fabrics (Launeau and Cruden, 1998). However, free grain rotation in a simple shear magma flow occurs periodically and is therefore not predictable (Launeau and Cruden, 1998). We thus consider it unlikely that *Fabric Type 2D* in the core of both discrete and coalesced magma fingers (II-3, JJ-1, Hb4, Hc8) reflects a similar timestep in the grain rotation cycle.

Sub-vertical magnetic foliations that are perpendicular to the magma finger long axis have been also observed in a previous study of a sill in the Karoo Igneous Province that is composed of multiple elongate elements (Hoyer and Watkeys, 2017). Hoyer and Watkeys (2017) interpreted these fabrics to reflect magma flow between coalesced elements, perpendicular to the intrusion long dimension. However, because *Type 2D* fabrics are also observed within discrete magma fingers (II-3, JJ-1) and due to the similarity in sample locations, we hypothesize that horizontal shortening parallel to the magma finger long axis due to the final intrusion tip arrest may have caused the formation of *Fabric Type 2D* (Figs. 13B–13C). Critically, the magma rheology has to enable viscous flow such that grains can rotate and overprint previously formed fabrics (e.g., Launeau and Cruden, 1998; Cañón-Tapia and Chávez-Álvarez, 2004). Crystallization and local solidification may therefore limit fabric overprinting to areas of localized magma flow. This could explain the occurrence of *Type 2C* and *2D* fabrics in the intrusion core and along the center line, which are plausible locations for localized magma flow during a late stage of magma emplacement (Figs. 13A–13B).

The moderately SE dipping foliation in sample Hbc5 is located close to the upper contact of the step that connects Fingers Hb and Hc (Fig. 10A). Here the magnetic foliation dips toward the frontal finger tip and may indicate imbrication of grains against the intrusion roof (e.g., Knight and Walker, 1988; Philpotts and Philpotts, 2007). In this case, Hbc5 records primary magma flow and the magnetic lineation oriented obliquely to the magma finger long axis may indicate local crossflow of magma between Fingers Hb and Hc (Fig. 13A).

5.3.4. Comparison of magnetic- and silicate petro-fabrics

The magnetic and silicate mineral foliations in samples Hbc6, Hc8, Hc9, Hc10, and Hc11 are broadly coincident (Fig. 11B). However, the maximum SPO direction of the silicate phases (V_1) plunges gently (2–28º) in these samples, which contrasts with the steep to sub-vertical orientation of K_1 (Fig. 11B; Tables 1 and 2). Angles between K_1 and V_1 axis orientations range from 44º (Hbc6) up to 75–88º (Hc7–Hc11). These differences may be caused by the presence of multiple silicate mineral sub-fabrics, which are averaged in the fabric tensor. For example, the orientation density distribution plots of samples Hc8 and Hc9 show girdles of long axes orientations with two distinct clusters (Fig. 11A). These clusters may reflect individual sub-fabrics and thus influence the average V_1 and V_2 fabric tensor orientations.

An alternative explanation for the different K_1 and V_1 orientations is the so-called "logjam" effect (Launeau and Cruden, 1998). This occurs when crystallizing silicate phases form a mineral framework in which individual grains start to interact during magma flow, preventing large grains from rotating and locking up or jamming the silicate petrofabric (Launeau and Cruden, 1998). At this stage, only smaller grains such as magnetite are able to rotate in response to continuing flow of the magma mush, although their degree of rotation will be limited by adjacent silicate grains (Launeau and Cruden, 1998). A relatively high degree of crystallization and a low volume percentage of melt (between ~30 and 50 %) are required to cause grain interaction and limit the rotation of silicate phases (Launeau and Cruden, 1998). Although the moderate modal concentration of silicate phenocrysts (~25–35 vol.%; Supplemental Material S5; Nash and Wilkinson, 1970) in our samples indicates a melt volume percentage of greater than 65 %, we suggest that the logjam model may explain some of the variations between magnetic and silicate petrofabrics, if the fabric overprinting occurred during a late stage of emplacement when the groundmass started to crystallize.

If the amount of late stage crystallization was high enough to cause interaction between individual grains, the logjam model may explain the ~74º discrepancy between K_1 and V_1 in sample JJ-2 (Fig. 9D). Sample JJ-2 is located close to the upper margin of Finger JJ, where both the magnetic and silicate petrofabric foliations are sub-parallel to the host rock contact (Fig. 9D). We therefore

interpret the foliations in sample JJ-2 to reflect the primary magma flow plane (e.g., Féménias et al., 2004). Given that the overall SE magma flow direction is constrained from field observations (Pollard et al., 1975), we interpret the NW-SE orientation of K_1 as primary flow indicator. The ~62º difference between V_1 and the finger long axis may indicate: (1) oblique flow of magma toward the lateral finger tip, which is suggested above to occur during intrusion widening (Figs. 2D, 13B); or (2) a stable orientation of silicate phases in a plane of constant magma velocity with V_1 oblique to the magma flow direction (e.g., Jeffery, 1922). We suggest that increased crystallization at the intrusion margins locked up the silicate petrofabrics that reflects either intrusion widening or stable grain orientations oblique to the magma flow, whereas magnetite grains remained mobile and re-aligned according to potential changes in magma flow kinematics.

The discrepancy between magnetic- and petro-fabric lineations could also be explained by intermediate magnetic fabrics, where K2 and K3 axis orientations are swapped (Rochette et al., 1999; Ferré et al., 2002). One indicator for potential intermediate magnetic fabrics are the coaxial fabric orientations, where K2 equals V3 and vice versa (JJ-2, Hc8–Hc11; Figs. 9D and 11B). If we assume intermediate magnetic fabrics in samples JJ-2 and Hc8–Hc11, the "corrected" magnetic fabrics would coincide with the petro-fabrics such that K1 in samples Hc9–Hc11 would approximately align in magma finger long dimension, resulting in Type 2A fabrics potentially indicating an interplay of magma flow along a steep boundary and horizontal finger widening (Figs. 13A–13B). The "corrected" K1 axis orientations in samples JJ-2 and Hc8 are sub-horizontal and trend approximately perpendicular to the magma finger long dimension, potentially reflecting an emplacement stage of magma finger widening. In sample Hc8, the sub-vertical magnetic foliation remains perpendicular to the magma finger long dimension which may still reflect NW-SE shortening (cf. Section 5.3.3). Although intermediate and/or inverse magnetic fabrics cannot be ruled out completely, our analyses suggest that the AMS data presented here likely reflect normal fabrics (cf. Section 5.1). We further note that V1 axis orientations are scattered and form girdles with multiple clusters in the orientation density distribution; these clusters potentially reflect individual sub-fabrics, such that the mean V1 axis orientation may not be meaningful.

5.4. The complexity of magma flow in finger-like intrusions

When magma flows in relatively thin sheets (<5 m), the resulting magnetic fabrics are more uniform than in thicker sheets, which can be due to: (1) magnetic fabrics in a larger part of the chilled margin in thinner sheets may record primary magma flow (e.g., Philpotts and Philpotts, 2007; Magee et al., 2016b); (2) thicker sheets have the potential to undergo thermal convection, which will overprint emplacement-related laminar flow fabrics (e.g., Holness et al., 2017); and (3) thicker sheets may comprise multiple magma pulses, with each pulse having its own magnetic fabric characteristics (e.g., Magee et al., 2016b). Although the magma fingers described here are relatively thin (~0.3–1.2 m), their magnetic fabrics show a range of fairly defined patterns and are not uniform (Fig. 13B). If magma flow in elongate elements is comparable to laminar fluid flow in a pipe, velocity profiles are expected to be axisymmetric with shapes that will vary depending on the fluid rheology (e.g., Pinho and Whitelaw, 1990). In such cases, imbricate fabrics are expected to form along the intrusion margin. However, cyclic particle rotation, a stable orientation of particles in a plane of constant magma velocity, or consecutive flow processes (i.e., primary magma flow and horizontal/vertical intrusion inflation) can overprint fabrics caused by laminar flow and may explain irregular fabrics in elements (e.g., Jeffery, 1922; Cañón-Tapia and Chávez-Álvarez, 2004). Due to the five distinct fabric patterns which are observed in similar sample locations in both individual and coalesced magma fingers, we consider it unlikely that these fabrics represent a similar stage of cyclic particle rotation. Instead, the distinct patterns in magnetic fabrics observed in the magma fingers suggest that: (1) magma flow in elongate elements is more complex than in planar sheet intrusions; and (2) magnetic fabrics record other syn-emplacement processes such as intrusion inflation rather than primary magma flow as discussed above (Fig. 13).

Syn-emplacement deformation of magnetic fabrics has been described in high-viscosity, felsic magmas, such as the Sandfell laccolith, Iceland (Mattsson et al., 2018). Here, magnetic fabrics were affected by S-C fabrics which formed in response to compression perpendicular to the intrusion contact and shearing during intrusion inflation; the magnetic foliation parallels the S-plane (i.e., foliation) whereas flow bands are parallel to C-planes (i.e., shear plane) (Mattsson et al., 2018). In a different scenario, magnetic fabrics within the felsic Cerro Bayo cryptodome, Argentina, deformed in response to multiple magma pulses, where intruding magma folded magma emplaced during previous pulses (Burchardt et al., 2019). These observations highlight an interplay between magnetic fabric orientation and syn-emplacement deformation. Importantly, this deformation is observed in felsic intrusions and fabric overprinting is controlled by high magma

viscosities, which enable the formation of syn-emplacement S-C structures or folding of previous magma pulses (Mattsson et al., 2018; Burchardt et al., 2019). These observations contrast with deformation of fabrics in low-viscosity intrusions, which we assign to an interplay of primary magma flow and both horizontal and vertical inflation, as described in this contribution. Dynamically changing flow regimes within elongate magma fingers may overprint primary flow fabrics multiple times, resulting in complex magnetic- and petro-fabrics.

5.5. Is flow in coalesced magma fingers sheet-like or localized?

Our data suggest that distinct emplacement processes operated during the intrusion of the Shonkin Sag magma fingers, associated with varying flow kinematics within coalesced magma fingers. These findings highlight the importance of sample locations and densities when interpreting magnetic- and petro-fabrics, especially within elongate elements and/or sheet intrusions comprising coalesced elements. We compared the fabric types observed in discrete (II and JJ) and coalesced (Hb and Hc) magma fingers and found that they reflect similar magma emplacement processes such as along-finger primary magma flow and both horizontal and/or vertical inflation. However, magnetic fabrics oriented oblique to the long axis of magma fingers Hb and Hc (Hb1, Hb3, Hbc5, Hbc6) suggest more complex and locally varying magma flow where magma fingers coalesce (Fig. 10B). Such complex flow patterns may result from: (1) oblique flow between adjacent magma fingers (Fig. 13A) (Hoyer and Watkeys, 2017; Martin et al., 2019); (2) locally turbulent flow due to the intrusion and connector geometry (Andersson et al., 2016); (3) flow localization due to closure of a connector caused by increased crystallinity (Holness and Humphreys, 2003; Magee et al., 2016b) (Fig. 13A); or (4) varying magma rheology, temperature, or velocity between the adjacent magma fingers (Magee et al., 2013, 2016b). Based on the data presented here, both sheet-like and localized magma flow in coalesced magma fingers is likely to have occurred. However, although samples within (Hbc5, Hbc6) and in the vicinity (Hb1, Hb3) to the step between Fingers Hb and Hc may be affected by local oblique magma flow between fingers, most of the fabrics observed in coalesced fingers are comparable to those in discrete examples. This suggests that along-magma finger flow and intrusion inflation within a coalesced finger remained considerably isolated and may imply a potential localized flow regime (Fig. 13A).

Identifying areas of sheet-like or localized magma flow within coalesced elements has implications for the emplacement of, and related magma flow pathways within sheet intrusions, which contributes to knowledge on sheet intrusion architecture and trans-crustal magma plumbing systems. These findings can be applied to the exploration of economic sulfide (Ni-Cu-Co-PGE) ore deposits, which are often linked to areas of both localized magma flow and high magma flux (e.g., Barnes et al., 2016). Localized, high magma flux can cause mechanical erosion and subsequent incorporation of the surrounding host rock into the magma, and as such, this process can contribute to accommodating the intruding magma and to increasing the crustal sulfur content (e.g., Gauert et al., 1996; Barnes et al., 2016). Understanding if and where in sheet intrusions magma flow may localize can therefore help to improve strategies for Ni-Cu-Co-PGE exploration.

On a crustal-scale, identifying flow kinematics within both individual and coalesced elements contributes to unravelling magma transport within large magma plumbing systems. For example, inclined to sub-vertical elements can act as feeders within interconnected sill networks, contributing to vertical magma transport (Guo et al., 2013; Magee et al., 2014). At shallow levels, this localized magma flow within elements and sheet intrusions may further result in horizontally distributed fissure eruptions at the Earth's surface. Understanding where in sheet intrusions magma flow can localize therefore is important for characterizing the architecture of and the internal magma transport within both individual and interconnected sheet intrusions.

6. Conclusions

We analyzed the AMS in four sample groups from the Shonkin Sag laccolith (Highwood Mountains, Montana, USA) and from samples from two isolated and two coalesced magma fingers that emerge from the laccolith's SE margin. The results suggest that the Shonkin Sag laccolith was fed by a NE-SW striking dyke, which is part of the swarm that radiates from the Highwood Mountains. The SE trending magma fingers at the SE margin of the laccolith are close to perpendicular to the inferred feeder-dyke. The AMS of samples from the magma fingers indicate magnetic fabrics that vary over short distances (i.e., less than 20 cm) that we interpret to reflect: (1) primary magma flow, which is mainly recorded in the upper and lower intrusion margins; and (2) syn-magmatic emplacement processes such as horizontal and/or vertical intrusion inflation,

which is mainly observed at the lateral tips and cores of the fingers. We classified five distinct fabric patterns, which we ascribe to fabric overprinting during different stages of magma finger emplacement, namely along-finger primary magma flow and intrusion inflation. Silicate petrofabric foliations obtained from high-resolution 3-D X-ray computed tomography data are similar to the magnetic fabrics determined for the magma fingers. Differences between magnetic fabric and petrofabric long axis orientations may result from increased crystallization, which results in grain interaction and jams up individual grains of the silicate framework, whereas small magnetite grains remain mobile and re-align according to magma emplacement processes. Within the connector between two coalesced magma fingers, magnetic lineation and foliation are oblique to the finger long axis, which suggests potential local crossflow between magma fingers once they are coalesced. Despite this local crossflow between coalesced fingers, magnetic fabrics suggest that magma flow may localize in each particular coalesced finger. The range of rock fabrics obtained from the magma fingers highlights the importance of sample locations when using AMS data to interpret primary magma flow. This is particularly important for elongate elements and sheet intrusions that comprise amalgamated elements, and has important implications for understanding their internal flow kinematics. The occurrence of distinct fabric types and fabric overprinting within a small area of a magma finger, as discussed in this contribution, may also imply that uniform data from larger sheet intrusions only reflect part of the intrusion emplacement history. This raises the question regarding at what point during intrusion emplacement the more complex fabric pattern are overprinted and become erased from the strain record? Our magnetic- and petro-fabric data reveal the interplay between competing forces during magma emplacement (i.e., along-finger flow and finger inflation), and imply processes that have been previously unrecognized. These magma emplacement processes and the overprinting of earlier magma flow kinematics should be considered when interpreting data from large-scale sheet intrusions.

Supplemental Material

Supplemental Material are available on doi.org/10.1016/j.jsg.2023.104829.

S0: 3D drone imagery of the studied outcrop

S1: Table with coordinates of sample locations

S2: Three component progressive thermal demagnetization of anhysteretic remanent magnetization (ARM)

S3: Table with AMS measurements of all individual specimens

S4: Table with SPO measurements of all individual grains

S5: Volume measurements of individual phases based on HRXRCT scans

S6: Raw BSE images of magnetite grain shown in Figure 4 I

Acknowledgments

We are grateful to the landowners Robert W. Ebeling, Holly Ebeling, and Jo Alice Juedeman for permitting access to the stunning cliff faces of the Shonkin Sag laccolith. We thank David Lageson for providing the portable drill used to collect rock samples. Drill holes in magma fingers produced during this study were subsequently infilled following the code of conduct for rock coring. We are grateful to Belinda Godel and Anja Slim for help with processing and analyzing HRXRCT data, Barbara Etschman for SEM analyses, and Uchitha Nissanka Arachchige for field assistance. We gratefully acknowledge helpful reviews by Steffi Burchardt and Sven Morgan, and we thank Ian Alsop for his editorial handling of the manuscript. JK acknowledges a Monash Graduate Scholarship and a Graduate Research Completion Award. ARC and CM acknowledge support from ARC Discovery Grant DP 190102422.

References

Akimoto, S., 1962. Magnetic properties of FeO-Fe2O3-TiO2 system as a basis of rock magnetism. Physical Society of Japan Journal 17, 706.

Anderson, E.M., 1951. The Dynamics of Faulting and Dyke Formation with Applications to Britain. Oliver and Boyd, Edinburgh, UK.

Anderson, E.M., 1937. The Dynamics of the Formation of Cone-sheets, Ring-dykes, and Caldron-subsidences. Proceedings of the Royal Society of Edinburgh 56, 128–157. https://doi.org/10.1017/S0370164600014954

Andersson, M., Almqvist, B.S.G., Burchardt, S., Troll, V.R., Malehmir, A., Snowball, I., Kübler, L., 2016. Magma transport in sheet intrusions of the Alnö carbonatite complex, central Sweden. Scientific Reports 6, 27635. https://doi.org/10.1038/srep27635

Barksdale, J.D., 1937. The Shonkin Sag laccolith. American Journal of Science 33, 321–359.

Barnes, S.J., Cruden, A.R., Arndt, N., Saumur, B.M., 2016. The mineral system approach applied to magmatic Ni–Cu–PGE sulphide deposits. Ore Geology Reviews 76, 296–316. https://doi.org/10.1016/j.oregeorev.2015.06.012

Buie, B.F., 1941. Igneous rocks of the Highwood Mountains, Montana: Part III. Dikes and Related Intrusives. Geological Society of America Bulletin 52, 1753–1808. https://doi.org/10.1130/GSAB-52-1753

Burchardt, S., Mattsson, T., Palma, J.O., Galland, O., Almqvist, B., Mair, K., Jerram, D.A., Hammer, Ø., Sun, Y., 2019. Progressive Growth of the Cerro Bayo Cryptodome, Chachahuén Volcano, Argentina—Implications for Viscous Magma Emplacement. Journal of Geophysical Research: Solid Earth 124, 7934–7961. https://doi.org/10.1029/2019JB017543

Burgess, C.H., 1941. Igneous rocks of the Highwood Mountains, Montana: Part IV. The Stocks. Geological Society of America Bulletin 52, 1809–1828.

Burton-Johnson, A., Macpherson, C.G., Muraszko, J.R., Harrison, R.J., Jordan, T.A., 2019. Tectonic strain recorded by magnetic fabrics (AMS) in plutons, including Mt Kinabalu, Borneo: A tool to explore past tectonic regimes and syn-magmatic deformation. Journal of Structural Geology 119, 50–60. https://doi.org/10.1016/j.jsg.2018.11.014

Cañón-Tapia, E., Chávez-Álvarez, J., 2004. Theoretical aspects of particle movement in flowing magma: implications for the anisotropy of magnetic susceptibility of dykes. Geological Society, London, Special Publications 238, 227–249. https://doi.org/10.1144/GSL.SP.2004.238.01.15

Cañón-Tapia, E., Herrero-Bervera, E., 2009. Sampling strategies and the anisotropy of magnetic susceptibility of dykes. Tectonophysics 466, 3–17. https://doi.org/10.1016/j.tecto.2008.11.012

Cashman, K.V., Sparks, R.S.J., 2013. How volcanoes work: A 25 year perspective. Bulletin of the Geological Society of America 125, 664–690. https://doi.org/10.1130/B30720.1

Cruden, A.R., Launeau, P., 1994. Structure, magnetic fabric and emplacement of the Archean Lebel Stock, SW Abitibi Greenstone Belt. Journal of Structural Geology 16, 766–691.

Cruden, A.R., Tobisch, O.T., Launeau, P., 1999. Magnetic fabric evidence for conduit-fed emplacement of a tabular intrusion: Dinkey Creek Pluton, central Sierra Nevada batholith, California. Journal of Geophysical Research: Solid Earth 104, 10,511-10,530. https://doi.org/10.1029/1998JB900093

Dunlop, D.J., Özdemir, Ö., 2001. Rock Magnetism: Fundamentals and frontiers, Cambridge Studies in Magnetism. Cambridge University Press, Cambridge; New York.

Eide, C.H., Schofield, N., Howell, J., Jerram, D.A., 2021. Transport of mafic magma through the crust and sedimentary basins: Jameson Land, East Greenland. Journal of the Geological Society jgs2021-043. https://doi.org/10.1144/jgs2021-043

Elliot, D.H., Fleming, T.H., 2004. Occurrence and dispersal of magmas in the Jurassic Ferrar Large Igneous Province, Antarctica. Gondwana Research 7, 223–237. https://doi.org/10.1016/S1342-937X(05)70322-1

Féménias, O., Diot, H., Berza, T., Gauffriau, A., Demaiffe, D., 2004. Asymmetrical to symmetrical magnetic fabric of dikes: Paleo-flow orientations and Paleo-stresses recorded on feeder-bodies from the Motru Dike Swarm (Romania). Journal of Structural Geology 26, 1401–1418. https://doi.org/10.1016/j.jsg.2003.12.003

Ferré, E.C., 2002. Theoretical models of intermediate and inverse AMS fabrics. Geophysical Research Letters 29, 31-1-31–4. https://doi.org/10.1029/2001GL014367

Ferré, E.C., Bordarier, C., Marsh, J.S., 2002. Magma flow inferred from AMS fabrics in a layered mafic sill, Insizwa, South Africa. Tectonophysics 354, 1–23. https://doi.org/10.1016/S0040-1951(02)00273-1

Galerne, C.Y., Galland, O., Neumann, E.R., Planke, S., 2011. 3D relationships between sills and their feeders: Evidence from the Golden Valley Sill Complex (Karoo Basin) and experimental modelling. Journal of Volcanology and Geothermal Research 202, 189–199. https://doi.org/10.1016/j.jvolgeores.2011.02.006

Galland, O., Spacapan, J.B., Rabbel, O., Mair, K., Soto, F.G., Eiken, T., Schiuma, M., Leanza, H.A., 2019. Structure, emplacement mechanism and magma-flow significance of igneous fingers – Implications for sill emplacement in sedimentary basins. Journal of Structural Geology 124, 120–135. https://doi.org/10.1016/j.jsg.2019.04.013

Gauert, C.D.K., Jordaan, L.J., de Waal, S.A., Wallmach, T., 1996. Isotopic constraints on the source of sulphur for the base metal sulphides of the Uitkomst Complex, Badplaas, South Africa. South African Journal of Geology 99, 41–50.

Gibb, F.G.F., Henderson, c. M.B., 1992. Convection and crystal settling in sills. Contributions to Mineralogy and Petrology 109, 538–545. https://doi.org/10.1007/BF00306555

Godel, B., 2013. High-resolution X-ray computed tomography and its application to ore deposits: From data acquisition to quantitative three-dimensional measurements with case studies from Ni-Cu-PGE Deposits. Economic Geology 108, 2005–2019. https://doi.org/10.2113/econgeo.108.8.2005

Hargraves, R.B., Johnson, D., Chan, C.Y., 1991. Distribution anisotropy: The cause of AMS in igneous rocks? Geophysical Research Letters 18, 2193–2196. https://doi.org/10.1029/91GL01777

Henderson, C.M.B., Richardson, F.R., Charnock, J.M., 2012. The Highwood Mountains potassic igneous province, Montana: mineral fractionation trends and magmatic processes revisited. Mineralogical Magazine 76, 1005–1051. https://doi.org/10.1180/minmag.2012.076.4.16

Holness, M.B., Humphreys, M.C.S., 2003. The Traigh Bhàn na Sgùrra Sill, Isle of Mull: Flow Localization in a Major Magma Conduit. Journal of Petrology 44, 1961–1976. https://doi.org/10.1093/petrology/egg066

Holness, M.B., Neufeld, J.A., Gilbert, A.J., Macdonald, R., 2017. Orientation of Tabular Mafic Intrusions Controls Convective Vigour and Crystallization Style. Journal of Petrology 58, 2035–2053. https://doi.org/10.1093/petrology/egx081

Horsman, E., Tikoff, B., Morgan, S., 2005. Emplacement-related fabric and multiple sheets in the Maiden Creek sill, Henry Mountains, Utah, USA. Journal of Structural Geology 27, 1426–1444. https://doi.org/10.1016/j.jsg.2005.03.003

Hoyer, L., Watkeys, M.K., 2017. Using magma flow indicators to infer flow dynamics in sills. Journal of Structural Geology 96, 161–175. https://doi.org/10.1016/j.jsg.2017.02.005

Hrouda, F., 1982. Magnetic anisotropy of rocks and its application in geology and geophysics. Geophysical Surveys 5, 37–82. https://doi.org/10.1007/BF01450244

Hurlbut Jr, C.S., 1939. Igneous rocks of the Highwood Mountains, Montana: Part I The laccoliths. Geological Society of America Bulletin 50, 1043–1112. https://doi.org/10.1130/GSAB-50-1043

Ildefonse, B., Launeau, P., Bouchez, J.-L., Fernandez, A., 1992. Effect of mechanical interactions on the development of shape preferred orientations: a two-dimensional experimental approach. Journal of Structural Geology 14, 73–83. https://doi.org/10.1016/0191-8141(92)90146-N

Jeffery, G.B., 1922. The motion of ellipsoidal particles immersed in a viscous fluid. Proceedings of the Royal Society of London. Series A, Containing Papers of a Mathematical and Physical Character 102, 161–179. https://doi.org/10.1098/rspa.1922.0078

Jelinek, V., 1981. Characterization of the magnetic fabric of rocks. Tectonophysics 79, 63–67. https://doi.org/10.1016/0040-1951(81)90110-4

Kendrick, G.C., Edmond, C.L., 1981. Magma immiscibility in the Shonkin Sag and Square Butte laccoliths. Geology 9, 615–619.

Khan, M.A., 1962. The anisotropy of magnetic susceptibility of some igneous and metamorphic rocks. Journal of Geophysical Research 67, 2873–2885. https://doi.org/10.1029/JZ067i007p02873

Knight, M.D., Walker, G.P.L., 1988. Magma flow directions in dikes of the Koolau Complex, Oahu, determined from magnetic fabric studies. Journal of Geophysical Research: Solid Earth 93, 4301–4319. https://doi.org/10.1029/JB093iB05p04301

Köpping, J., Magee, C., Cruden, A.R., Jackson, C.A.-L., Norcliffe, J.R., 2022. The building blocks of igneous sheet intrusions: Insights from 3-D seismic reflection data. Geosphere. https://doi.org/10.1130/GES02390.1

Larsen, E.S., 1941. Igneous rocks of the Highwood Mountains, Montana: Part II. The Extrusive Rocks. Geological Society of America Bulletin 52, 1733–1752. https://doi.org/10.1130/GSAB-52-1733

Launeau, P., Cruden, A.R., 1998. Magmatic fabric acquisition mechanisms in a syenite: Results of a combined anisotropy of magnetic susceptibility and image analysis study. Journal of Geophysical Research 103, 5067–5089. https://doi.org/10.1029/97JB02670

Leat, P.T., 2008. On the long-distance transport of Ferrar magmas. Geological Society Special Publication 302, 45–61. https://doi.org/10.1144/SP302.4

Leite, R.J., 1959. An experimental investigation of the stability of Poiseuille flow. Journal of Fluid Mechanics 5, 81. https://doi.org/10.1017/S0022112059000076

Lowrie, W., 1990. Identification of ferromagnetic minerals in a rock by coercivity and unblocking temperature properties. Geophysical Research Letters 17, 159–162. https://doi.org/10.1029/GL017i002p00159

Magee, C., Muirhead, J., Schofield, N., Walker, R.J., Galland, O., Holford, S., Spacapan, J., Jackson, C.A.L., McCarthy, W., 2019. Structural signatures of igneous sheet intrusion propagation. Journal of Structural Geology 125, 148–154. https://doi.org/10.1016/j.jsg.2018.07.010

Magee, C., Muirhead, J.D., Karvelas, A., Holford, S.P., Jackson, C.A.L., Bastow, I.D., Schofield, N., Stevenson, C.T.E., McLean, C., McCarthy, W., Shtukert, O., 2016a. Lateral magma flow in mafic sill complexes. Geosphere 12, 1–33. https://doi.org/10.1130/GES01256.1

Magee, C., O'Driscoll, B., Petronis, M.S., Stevenson, C.T.E., 2016b. Three-dimensional magma flow dynamics within subvolcanic sheet intrusions. Geosphere 12, 842–866. https://doi.org/10.1130/GES01270.1

Magee, C., O'Driscoll, B., Petronis, M.S., Stevenson, C.T.E., Clay, P.L., Gertisser, R., 2013. Magma rheology variations in sheet intrusions of the Ardnamurchan Central Complex (Scotland) inferred from gabbro inclusion characteristics. Journal of Petrology 54, 75–102. https://doi.org/10.1093/petrology/egs064

Martin, S.A., Kavanagh, J.L., Biggin, A.J., Utley, J.E.P., 2019. The origin and evolution of magnetic fabrics in mafic sills. Frontiers in Earth Science 7, 1–23. https://doi.org/10.3389/feart.2019.00064

Marvin, R.F., Hearn Jr., B.O., Mehnert, H.H., Naesser, C.W., Zartman, R.E., Lindsley, D.A., 1980. Late Cretaceous-Paleocene igneous activity in north-central Montana. Isochron/West 29, 5–25.

Mattsson, T., Burchardt, S., Almqvist, B.S.G., Ronchin, E., 2018. Syn-Emplacement Fracturing in the Sandfell Laccolith, Eastern Iceland—Implications for Rhyolite Intrusion Growth and Volcanic Hazards. Frontiers in Earth Science 6. https://doi.org/10.3389/feart.2018.00005

Mattsson, T., Petri, B., Almqvist, B., McCarthy, W., Burchardt, S., Palma, J.O., Hammer, Ø., Galland, O., 2021. Decrypting Magnetic Fabrics (AMS, AARM, AIRM) Through the Analysis of Mineral Shape Fabrics and Distribution Anisotropy. Journal of Geophysical Research: Solid Earth 126, e2021JB021895. https://doi.org/10.1029/2021JB021895

McCarthy, W., Petronis, M.S., Reavy, R.J., Stevenson, C.T., 2015. Distinguishing diapirs from inflated plutons: an integrated rock magnetic fabric and structural study on the Roundstone Pluton, western Ireland. Journal of the Geological Society 172, 550–565. https://doi.org/10.1144/jgs2014-067

Merle, O., 2000. Numerical modelling of strain in lava tubes. Bulletin of Volcanology 62, 53–58. https://doi.org/10.1007/s004450050290

Montana Bureau of Mines and Geology [WWW Document], 2021. Montana Geologic Maps. URL https://www.mbmg.mtech.edu/Information/StoryMaps/GeologicMaps.asp (accessed 10.4.21).

Morgan, S., 2018. Chapter 6 - Pascal's Principle, a Simple Model to Explain the Emplacement of Laccoliths and Some Mid-crustal Plutons. In: Burchardt, S. (Ed.), Volcanic and Igneous Plumbing Systems. Elsevier, 139–165. https://doi.org/10.1016/B978-0-12-809749-6.00006-6

Morgan, S., Jones, R., Conner, J., Student, J., Schaner, M., Horsman, E., de Saint Blanquat, M., 2017. Magma sheets defined with magnetic susceptibility in the Maiden Creek sill, Henry Mountains, Utah, USA. Geology 45, 599–602. https://doi.org/10.1130/G38932.1

Morgan, S., Stanik, A., Horsman, E., Tikoff, B., de Saint Blanquat, M., Habert, G., 2008. Emplacement of multiple magma sheets and wall rock deformation: Trachyte Mesa intrusion, Henry Mountains, Utah. Journal of Structural Geology 30, 491–512. https://doi.org/10.1016/j.jsg.2008.01.005

Muirhead, J.D., Airoldi, G., Rowland, J.V., White, J.D.L., 2012. Interconnected sills and inclined sheet intrusions control shallow magma transport in the Ferrar large igneous province, Antarctica. Geological Society of America Bulletin 124, 162–180. https://doi.org/10.1130/B30455.1

Nash, W.P., Wilkinson, J.F.G., 1971. Shonkin Sag laccolith, Montana: II. Bulk rock geochemistry. Contributions to Mineralogy and Petrology 33, 162–170. https://doi.org/10.1007/BF00386113

Nash, W.P., Wilkinson, J.F.G., 1970. Shonkin Sag laccolith, Montana: I. Mafic minerals and estimates of temperature, pressure, oxygen fugacity and silica activity. Contributions to Mineralogy and Petrology 25, 241–269. https://doi.org/10.1007/BF00399286

O'Brien, H.E., Irving, A.J., McCallum, I.S., 1991. Eocene potassic magmatism in the Highwood Mountains, Montana: petrology, geochemistry, and tectonic implications. Journal of Geophysical Research 96. https://doi.org/10.1029/91jb00599

O'Driscoll, B., Stevenson, C.T.E., Troll, V.R., 2008. Mineral Lamination Development in Layered Gabbros of the British Palaeogene Igneous Province: A Combined Anisotropy of Magnetic Susceptibility, Quantitative Textural and Mineral Chemistry Study. Journal of Petrology 49, 1187–1221. https://doi.org/10.1093/petrology/egn022

Osborne, F.F., Roberts, E.J., 1931. Differentiation in the Shonkin Sag laccolith, Montana. American Journal of Science 5, 331–353.

Petri, B., Almqvist, B.S.G., Pistone, M., 2020. 3D rock fabric analysis using micro-tomography: An introduction to the open-source TomoFab MATLAB code. Computers & Geosciences 138, 104444. https://doi.org/10.1016/j.cageo.2020.104444

Philpotts, A.R., Asher, P.M., 1994. Magmatic flow-direction indicators in a giant diabase feeder dike, Connecticut. Geology 22, 363–366. https://doi.org/10.1130/0091-7613(1994)022<0363:MFDIIA>2.3.CO;2

Philpotts, A.R., Philpotts, D.E., 2007. Upward and downward flow in a camptonite dike as recorded by deformed vesicles and the anisotropy of magnetic susceptibility (AMS). Journal of Volcanology and Geothermal Research 161, 81–94. https://doi.org/10.1016/j.jvolgeores.2006.11.006

Pinho, F.T., Whitelaw, J.H., 1990. Flow of non-newtonian fluids in a pipe. Journal of Non-Newtonian Fluid Mechanics 34, 129–144. https://doi.org/10.1016/0377-0257(90)80015-R

Pirsson, L.V., 1905. Petrography and geology of the igneous rocks of the Highwood Mountains, Montana. US Geological Survey Bulletin 237, 1–207.

Poland, M.P., Fink, J.H., Tauxe, L., 2004. Patterns of magma flow in segmented silicic dikes at Summer Coon volcano, Colorado: AMS and thin section analysis. Earth and Planetary Science Letters 219, 155–169. https://doi.org/10.1016/S0012-821X(03)00706-4

Pollard, D.D., Muller, O.H., Dockstader, D.R., 1975. The form and growth of fingered sheet intrusions. Geological Society of America Bulletin 86, 351–363. https://doi.org/10.1130/0016-7606(1975)86<351:TFAGOF>2.0.CO;2

Potter, D.K., Stephenson, A., 1988. Single-domain particles in rocks and magnetic fabric analysis. Geophysical Research Letters 15, 1097–1100. https://doi.org/10.1029/GL015i010p01097

Rickwood, P.C., 1990. The anatomy of a dyke and the determination of propagation and magma flow directions. In: Parker, A.J., Rickwood, P.C., Tucker, D.H. (Eds.), Mafic Dykes and Emplacement Mechanisms. Balkeme, Rotterdam, 81–100.

Riller, U., Cruden, A.R., Schwerdtner, W.M., 1996. Magnetic fabric and microstructural evidence for a tectono-thermal overprint of the early Proterozoic Murray pluton, central Ontario, Canada. Journal of Structural Geology 18, 1005–1016. https://doi.org/10.1016/0191-8141(96)00028-4

Rochette, P., Aubourg, C., Perrin, M., 1999. Is this magnetic fabric normal? A review and case studies in volcanic formations. Tectonophysics 307, 219–234. https://doi.org/10.1016/S0040-1951(99)00127-4

Rochette, P., Fillion, G., 1988. Identification of multicomponent anisotropies in rocks using various field and temperature values in a cryogenic magnetometer. Physics of the Earth and Planetary Interiors 51, 379–386. https://doi.org/10.1016/0031-9201(88)90079-9

Roni, E., Westerman, D.S., Dini, A., Stevenson, C., Rocchi, S., 2014. Feeding and growth of a dyke–laccolith system (Elba Island, Italy) from AMS and mineral fabric data. Journal of the Geological Society 171, 413–424. https://doi.org/10.1144/jgs2013-019

Ruggles, C.E., Morgan, S., Reber, J.E., 2021. A multiple-pulse emplacement model for the Shonkin Sag laccolith, Montana, USA. Journal of Structural Geology 149, 104378. https://doi.org/10.1016/j.jsg.2021.104378

Schofield, N., Holford, S., Millett, J., Brown, D., Jolley, D., Passey, S.R., Muirhead, D., Grove, C., Magee, C., Murray, J., Hole, M., Jackson, C.A.L., Stevenson, C., 2017. Regional magma plumbing and emplacement mechanisms of the Faroe-Shetland Sill Complex: implications for magma transport and petroleum systems within sedimentary basins. Basin Research 29, 41–63. https://doi.org/10.1111/bre.12164

Schofield, N.J., Brown, D.J., Magee, C., Stevenson, C.T., 2012a. Sill morphology and comparison of brittle and non-brittle emplacement mechanisms. Journal of the Geological Society 169, 127–141. https://doi.org/10.1144/0016-76492011-078

Schofield, N.J., Heaton, L., Holford, S.P., Archer, S.G., Jackson, C.A.-L., Jolley, D.W., 2012b. Seismic imaging of 'broken bridges': linking seismic to outcrop-scale investigations of intrusive magma lobes. Journal of the Geological Society 169, 421–426. https://doi.org/10.1144/0016-76492011-150

Spacapan, J.B., Galland, O., Leanza, H.A., Planke, S., 2017. Igneous sill and finger emplacement mechanism in shale-dominated formations: a field study at Cuesta del Chihuido, Neuquén Basin, Argentina. Journal of the Geological Society 174, 422–433. https://doi.org/10.1144/jgs2016-056

Sparks, R.S.J., 2003. Forecasting volcanic eruptions. Earth and Planetary Science Letters 210, 1–15. https://doi.org/10.1016/S0012-821X(03)00124-9

Stacey, F.D., 1960. Magnetic anisotropy of igneous rocks. Journal of Geophysical Research (1896-1977) 65, 2429–2442. https://doi.org/10.1029/JZ065i008p02429

Stephens, T., Walker, R., Healy, D., Bubeck, A., 2021. Segment tip geometry of sheet intrusions, II: Field observations of tip geometries and a model for evolving emplacement mechanisms. Volcanica 4, 203–225. https://doi.org/10.30909/vol.04.02.203225

Tarling, D., Hrouda, F., 1993. Magnetic anisotropy of rocks. New York, Chapman and Hall.

Tauxe, L., 2003. Paleomagnetic Principles and Practice, Modern Approaches in Geophysics. Springer, Dordrecht.

Trippanera, D., Porreca, M., Urbani, S., Kissel, C., Winkler, A., Sagnotti, L., Nazzareni, S., Acocella, V., 2020. Interpreting Inverse Magnetic Fabric in Miocene Dikes From Eastern Iceland. Journal of Geophysical Research: Solid Earth 125, e2020JB020306. https://doi.org/10.1029/2020JB020306

Vollmer, F.W., 1995. C program for automatic contouring of spherical orientation data using a modified Kamb method. Computers & Geosciences 21, 31–49. https://doi.org/10.1016/0098-3004(94)00058-3

Walker, R., Stephens, T., Greenfield, C., Gill, S., Healy, D., Poppe, S., 2021. Segment tip geometry of sheet intrusions, I: Theory and numerical models for the role of tip shape in controlling propagation pathways. Volcanica 4, 189–201. https://doi.org/10.30909/vol.04.02.189201

Weed, W.H., Pirsson, L.V., 1895. Highwood Mountains of Montana. Bulletin of the Geological Society of America 6, 389–422. https://doi.org/10.1130/GSAB-6-389

Wilson, P.I.R., McCaffrey, K.J.W., Wilson, R.W., Jarvis, I., Holdsworth, R.E., 2016. Deformation structures associated with the Trachyte Mesa intrusion, Henry Mountains, Utah: Implications for sill and laccolith emplacement mechanisms. Journal of Structural Geology 87, 30–46. https://doi.org/10.1016/j.jsg.2016.04.001

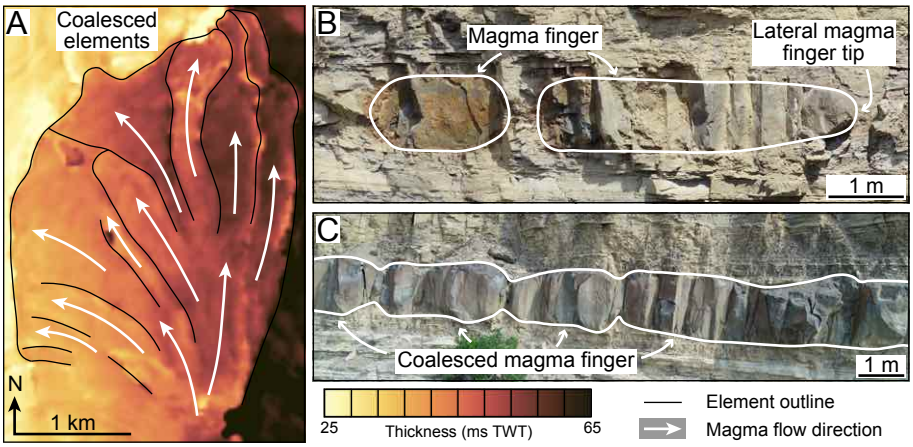

Figure 1: (A) Coalesced, elongate elements highlighted in 3-D seismic reflection data of a sill located offshore NW Australia (Köpping et al., 2022). Thickness map shows distinct thickness variations between adjacent elements. (B) Discrete magma fingers at the SE margin of the Shonkin Sag laccolith, Montana, USA (Pollard et al., 1975). (C) Coalesced magma fingers form a continuous sheet intrusion at the SE margin of the Shonkin Sag laccolith, Montana, USA (Pollard et al., 1975).

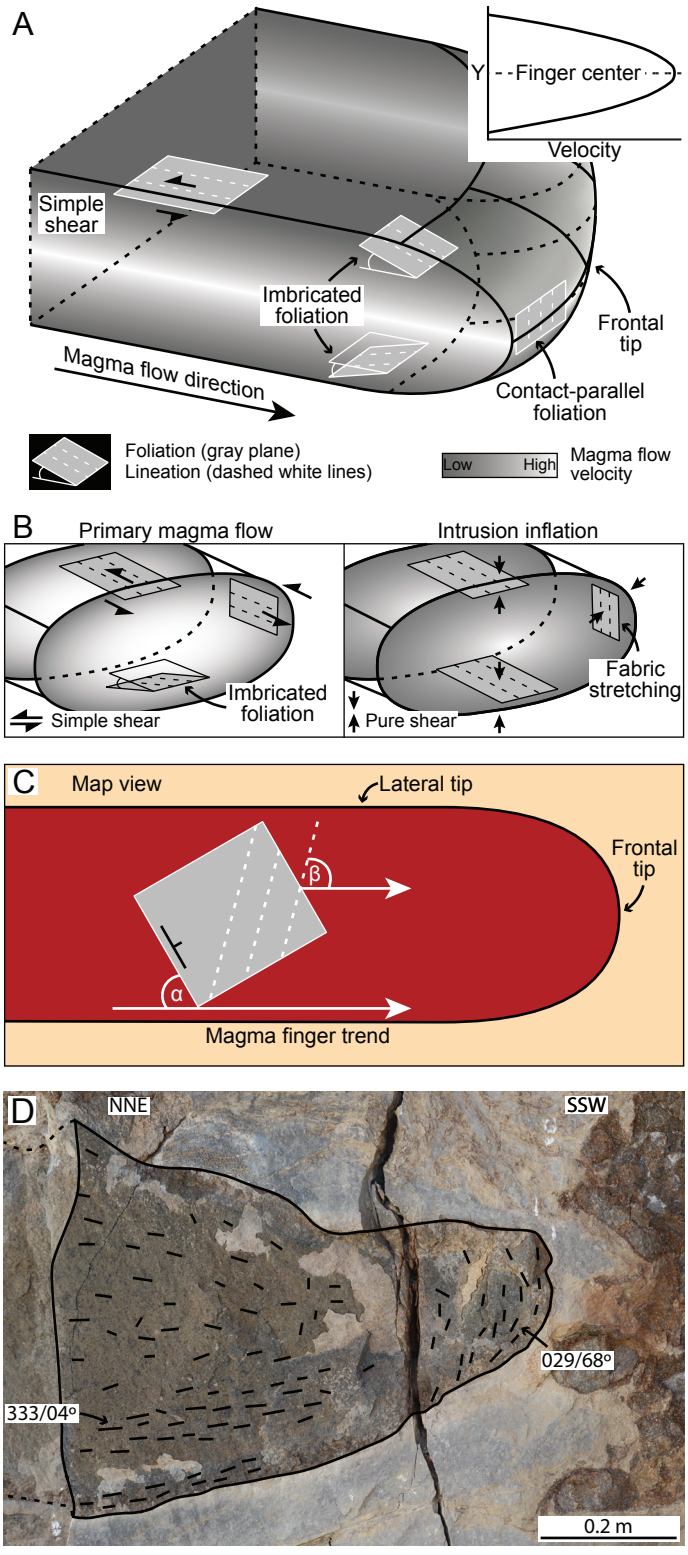

Figure 2: (A) Schematic diagram illustrates magma flow within igneous intrusions and highlights potential flow fabrics (modified after Magee et al., 2016). (B) Schematic diagrams illustrate expected fabrics resulted from primary magma flow and both vertical and horizontal magma finger inflation. (C) Schematic diagram shows the angular relation between both the foliation and lineation and the trend of magma fingers; α defines the angle between the foliation

strike and the magma finger trend, and β defines the angle between the lineation and the magma finger trend. (D) Field photograph of a lateral magma finger tip located at the SE margin of the Shonkin Sag laccolith (Montana, USA). Black lines indicate the maximum shape preferred orientation of clinopyroxene phenocrysts and show the alignment of minerals sub-parallel to the intrusion-host rock contact.

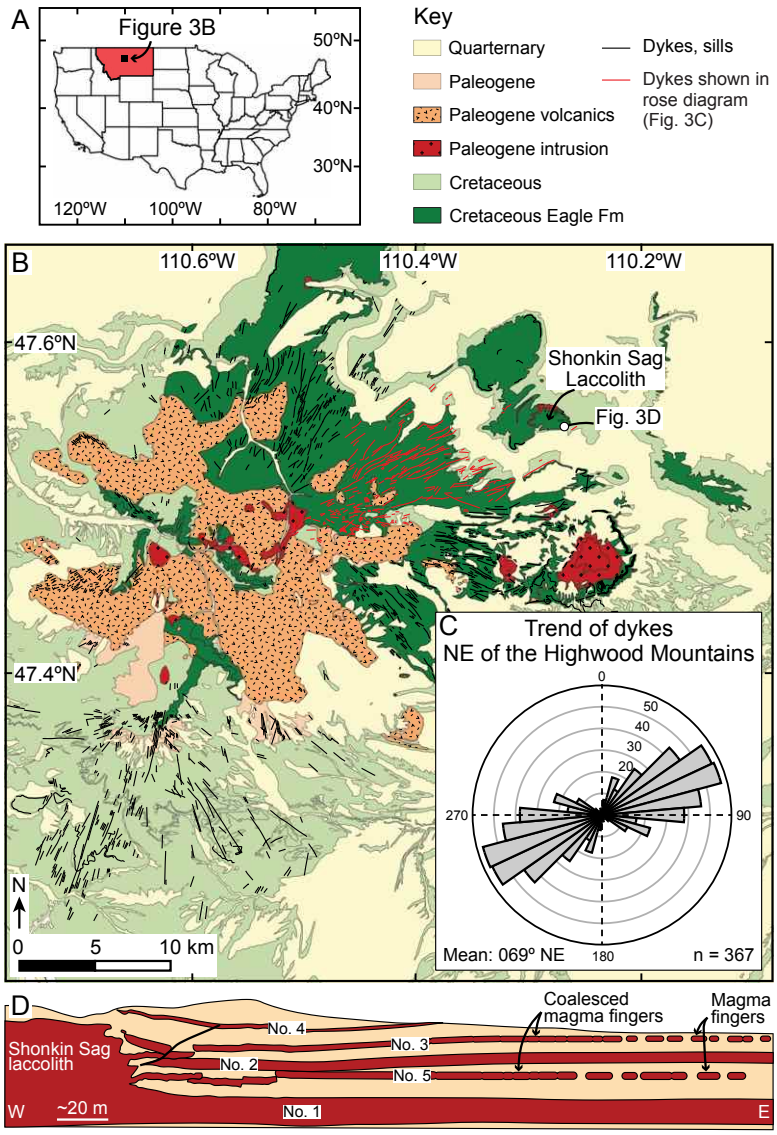

Figure 3: Location maps of study area. (A) Overview map shows the location of the Highwood Mountains, Montana, USA. (B) Simplified geological map indicates sedimentary, volcanic, and igneous rocks of the Highwood Mountains (based on the Geological Map of the quadrangles 'Fort Benton' and 'Belt'; 1:100,000 scale; available from the Montana Bureau of Mines and Geology (2021)). Field examples of magma fingers are shown in Figures 1B and 1C. (C) Rose diagram shows the trend of dykes that crop out NE of the Highwood Mountains (color-coded in red in Figure 3B). (D) Schematic diagram of a cliff face located at the southeast Shonkin Sag laccolith margin shows the transition of the laccolith into 5 emerging sills. Sills No. 3 and No. 5 show evidence of both coalesced and discrete magma fingers. Note that magma fingers indicated in the cross section are schematic and do not represent the accurate size or

location. Sample locations and drone imagery of the outcrop are provided in Supplemental Material S0–S1. The cross section location is indicated in Figure 3B.

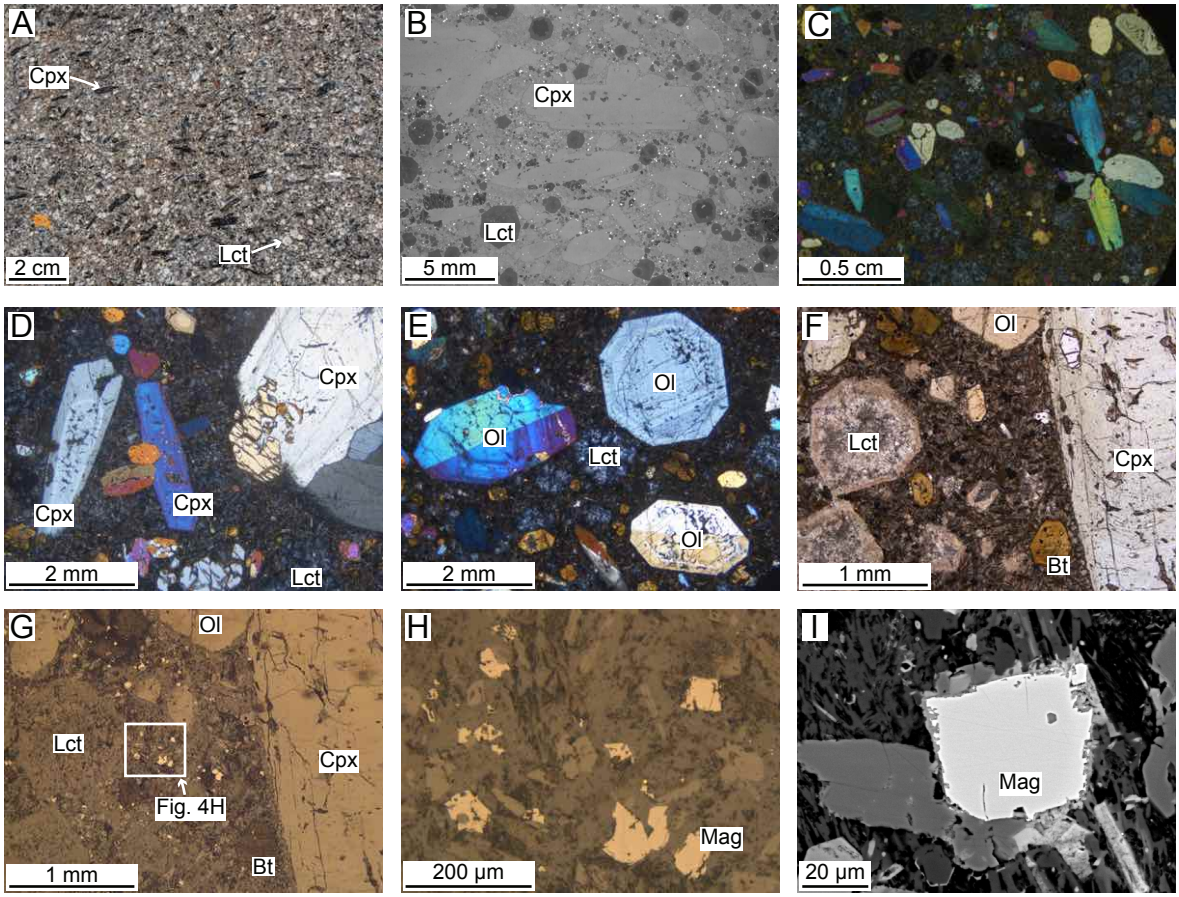

Figure 4: (A) Field photograph and (B) HRXRCT scan of shonkinite from magma fingers at the SE Shonkin Sag laccolith margin. Note the shape preferred orientation of Cpx. Cpx–clinopyroxene; Lct–leucite. (C–H) Photomicrographs of shonkinite under (C–E) crossed-polarized light, (F) plane-polarized light, and (G, H) reflected light. Ol–olivine; Bt–biotite; Mag–magnetite. (I) Backscattered electron image of a magnetite grain. Note that two images with different brightness-level were merged to visualize the internal magnetite structure and the groundmass. Raw-images are shown in the Supplemental Material S6.

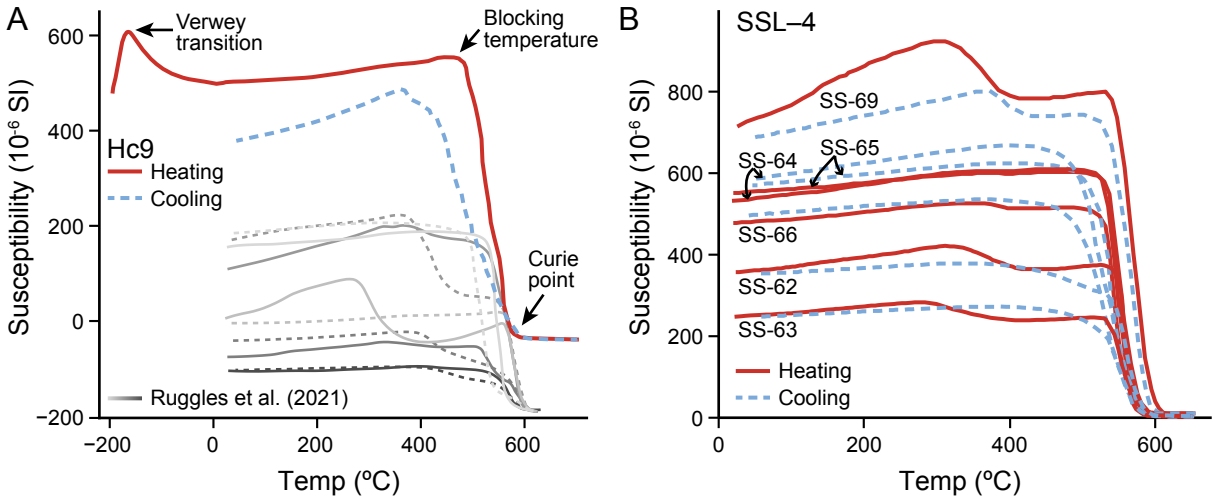

Figure 5: Low-to-high temperature, low-field susceptibility experiment of (A) a sample collected within magma finger Hc (Hc9) and (B) samples collected along a vertical transect through the Shonkin Sag laccolith (SSL-4). Arrows in (A) indicate the Verwey transition (-165 ºC), blocking temperature (483 ºC), and the Curie point (570 ºC). Gray lines in (A) show data from samples collected from the Shonkin Sag laccolith and emerging sills as presented by Ruggles et al. (2021). Continuous and dashed lines indicate heating and cooling curves, respectively. (B) Specimens of sample group SSL-4 have blocking temperatures at about 520–530 ºC and Curie points occur between 580–605 ºC.

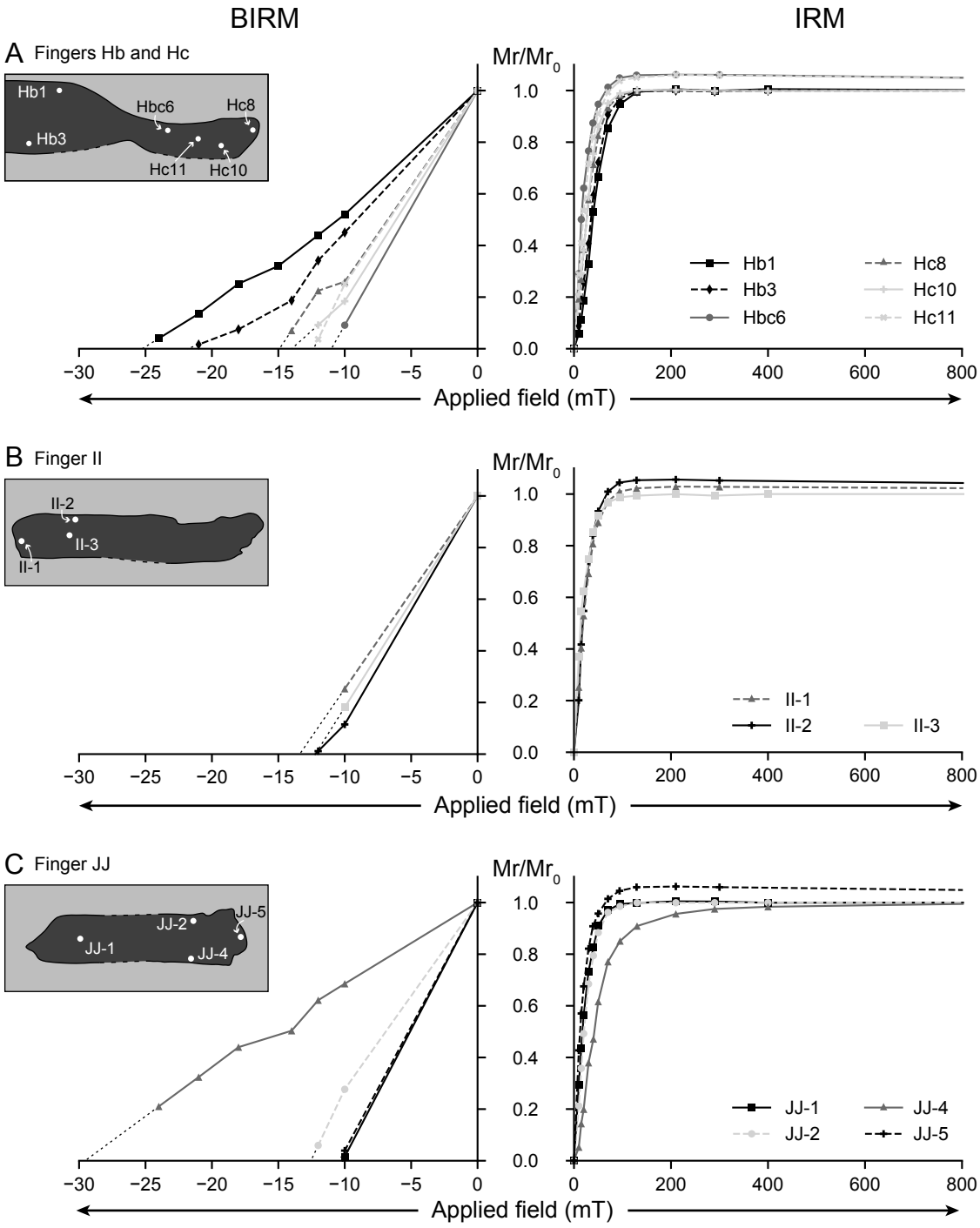

Figure 6: Results of isothermal remanent magnetization (IRM) and back-field IRM (BIRM) demagnetization experiments for samples in (A) fingers Hb and Hc, (B) finger II, and (C) finger JJ. Black dashed lines in BIRM plots are extrapolated BIRM curves which are used to estimate the coercivity of remanence (H_{CR}). Schematic diagrams of magma fingers indicate the sample location (white dots).

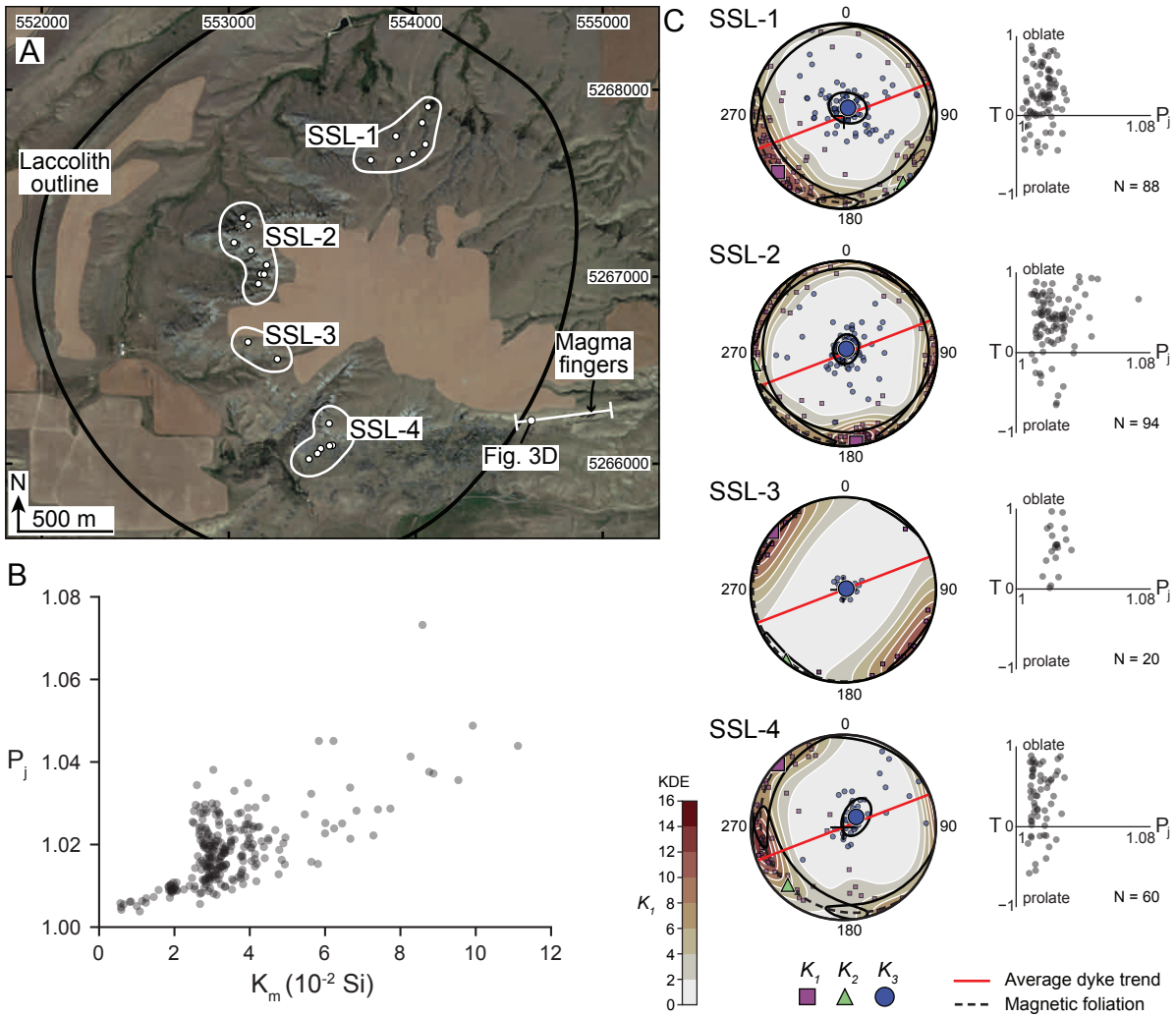

Figure 7: (A) Satellite image (GoogleEarth) of the Shonkin Sag laccolith shows the sample locations of sample group SSL-1–SSL-4 (white dots) and the location of magma fingers at the SE laccolith margin; laccolith outline after Hurlbut Jr. (1939). (B) Plot of the mean magnetic susceptibility (Km) against the corrected degree of anisotropy (Pj) for all specimens. (C) Equal-area lower hemisphere stereonet plots of the anisotropy of magnetic susceptibility (AMS) for the four sample groups. 95% confidence ellipses are plotted for the average principal susceptibility axes. Orientation density distribution contours are visualized for K1 axes. Red lines indicate the average trend (069º NE) of dykes NE of the Highwood Mountains, as is shown in Fig. 3C. Pj is plotted against the shape parameter (T) for each sample group.

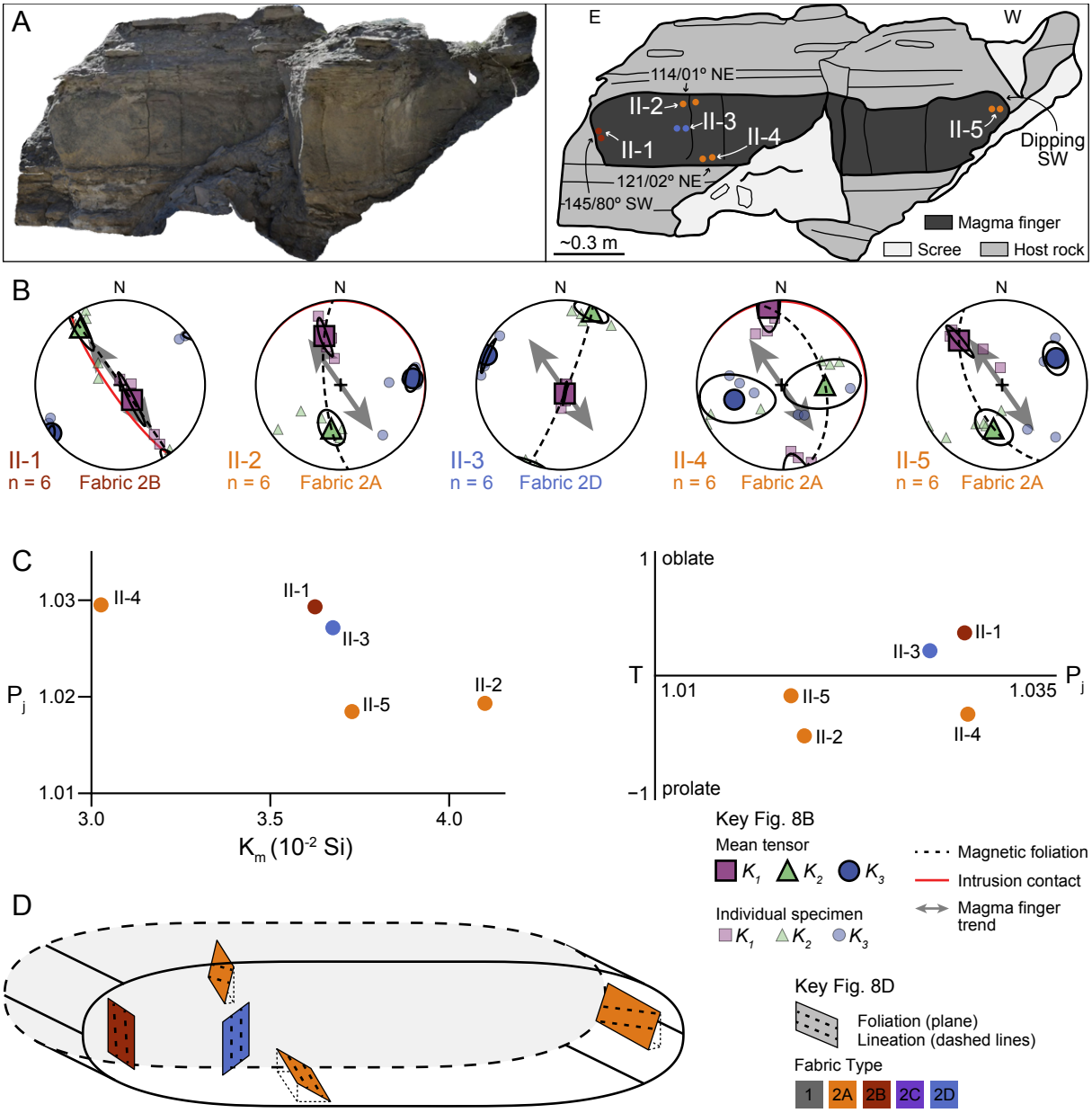

Figure 8: (A) Photomosaic and interpreted sketch for magma finger II. Dots are color-coded for the fabric type and highlight the individual sample locations, and structural measurements (strike/dip) indicate the intrusion-host rock contact. (B) Equal-area, lower hemisphere stereonet plots of the anisotropy of magnetic susceptibility (AMS) for the five sample locations (II-1–II-5) shown in (A). 95% confidence ellipses are plotted for the average principal susceptibility axes. The magma finger trend (145° SE; gray arrow) is inferred from the intrusion-host rock contact at the lateral E finger tip (145/80° SW). (C) Plots for the corrected degree of anisotropy (P_j) against both the mean magnetic susceptibility (K_m) and the shape factor (T). Note that the plotted measurements are mean values for each sample location in finger II. (D) Schematic

diagram shows the magnetic fabric orientation at the approximate sample location within magma finger II.

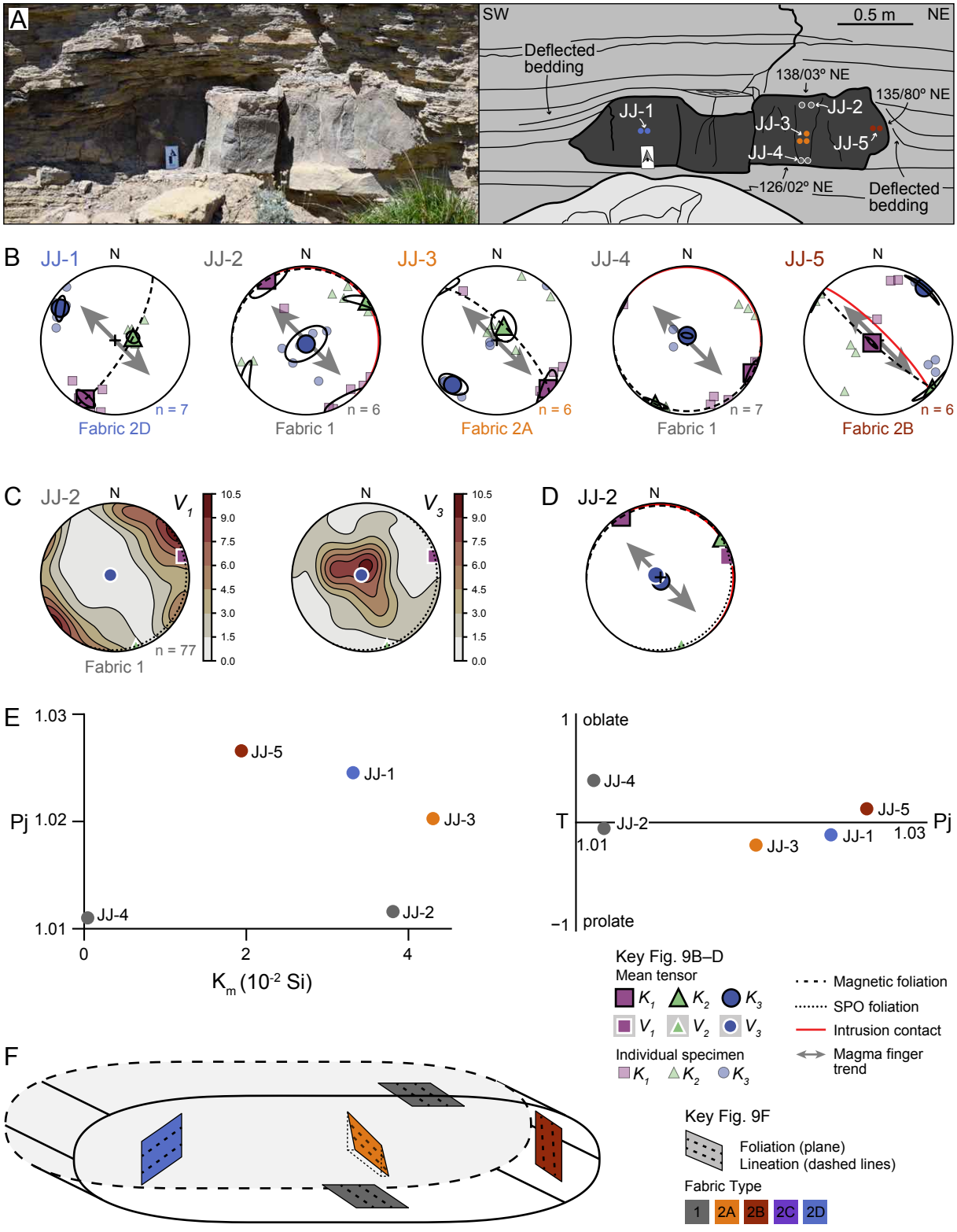

Figure 9: (A) Photograph and interpreted sketch for magma finger JJ. Dots are color-coded for the fabric type and highlight the individual sample locations, and structural measurements (strike/dip) indicate the intrusion-host rock contact. (B) Equal-area, lower hemisphere stereonet plots of the anisotropy of magnetic susceptibility (AMS) for the five sample locations (JJ-1–

JJ-5) shown in (A). 95% confidence ellipses are plotted for the average principal susceptibility axes. The magma finger trend (135º SE; gray arrow) is inferred from the intrusion-host rock contact at the lateral NE finger tip (135/80º NE). (C) Equal-area, lower hemisphere stereonet plots show the orientation density distribution of long axes (V_1) and short axes (V_3) orientations of clinopyroxene and olivine crystals in JJ-2; average fabric tensor axes orientations (V_1, V_2, V_3) are indicated. (D) Equal-area, lower hemisphere stereonet plot shows the comparison of AMS (K_1, K_2, K_3) and fabric tensor (V_1, V_2, V_3) axes orientations. (E) Plots for the corrected degree of anisotropy (P_j) against both the mean magnetic susceptibility (K_m) and the shape factor (T). Note that the plotted measurements are mean values for each sample location in finger JJ. (F) Schematic diagram shows the magnetic fabric orientation at the approximate sample location within magma finger JJ.

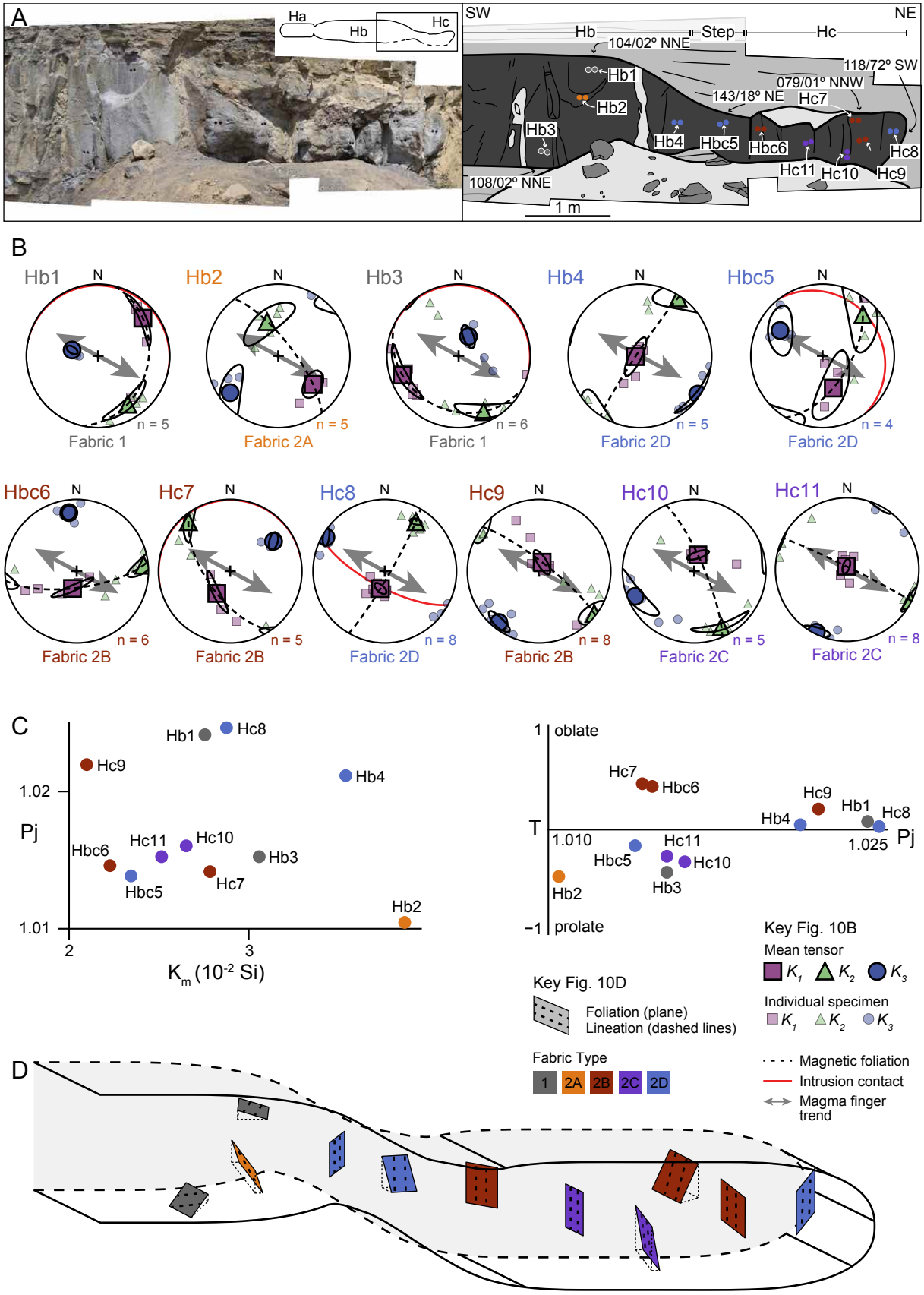
A
Ha
Hb
Hc
SW
NE
Hb
Step
Hc
104/02° NNE
118/72° SW
079/01° NNW
143/18° NE
Hc7
Hb1
Hb2
Hb3
Hb4
Hbc5
Hbc6
Hc8
Hc11
Hc10
Hc9
108/02° NNE
1 m
B
Hb1
Hb2
Hb3
Hb4
Hbc5
N
n = 5
Fabric 1
n = 5
Fabric 2A
n = 6
Fabric 1
n = 5
Fabric 2D
n = 4
Fabric 2D
Hbc6
Hc7
Hc8
Hc9
Hc10
Hc11
n = 6
Fabric 2B
n = 5
Fabric 2B
n = 8
Fabric 2D
n = 8
Fabric 2B
n = 5
Fabric 2C
n = 8
Fabric 2C
C
Hb1
Hc8
Hc9
Hb4
1.02
Pj
Hbc6
Hc11
Hc10
Hb3
Hbc5
Hc7
Hb2
1.01
2
3
K_m (10^-2 Si)
1
oblate
Hc7
Hbc6
Hc9
Hb1
Hc8
Hb4
T
1.010
Hc11
Hbc5
Hc10
Hb3
Hb2
1.025
Pj
−1
prolate
Key Fig. 10B
Mean tensor
K1 K2 K3
Individual specimen
K1 K2 K3
Key Fig. 10D
Foliation (plane)
Lineation (dashed lines)
Fabric Type
1
2A
2B
2C
2D
Magnetic foliation
Intrusion contact
Magma finger trend
D

Figure 10: (A) Photomosaic and interpreted sketch for magma fingers Hb and Hc. Dots are color-coded for the fabric type and highlight the individual sample locations, and structural measurements (strike/dip) indicate the intrusion-host rock contact. (B) Equal-area, lower hemisphere stereonet plots of the anisotropy of magnetic susceptibility (AMS) for the eleven sample locations (Hb1–Hc11) shown in (A). 95% confidence ellipses are plotted for the average principal susceptibility axes. The magma finger trend (118º SE; gray arrow) is inferred from the intrusion-host rock contact at the lateral NE finger tip of Hc (118/72º SW). (C) Plots for the corrected degree of anisotropy (P_j) against both the mean magnetic susceptibility (K_m) and the shape factor (T). Note that the plotted measurements are mean values for each sample location in fingers Hb and Hc. (D) Schematic diagram shows the magnetic fabric orientation at the approximate sample location within the coalesced magma fingers Hb and Hc.

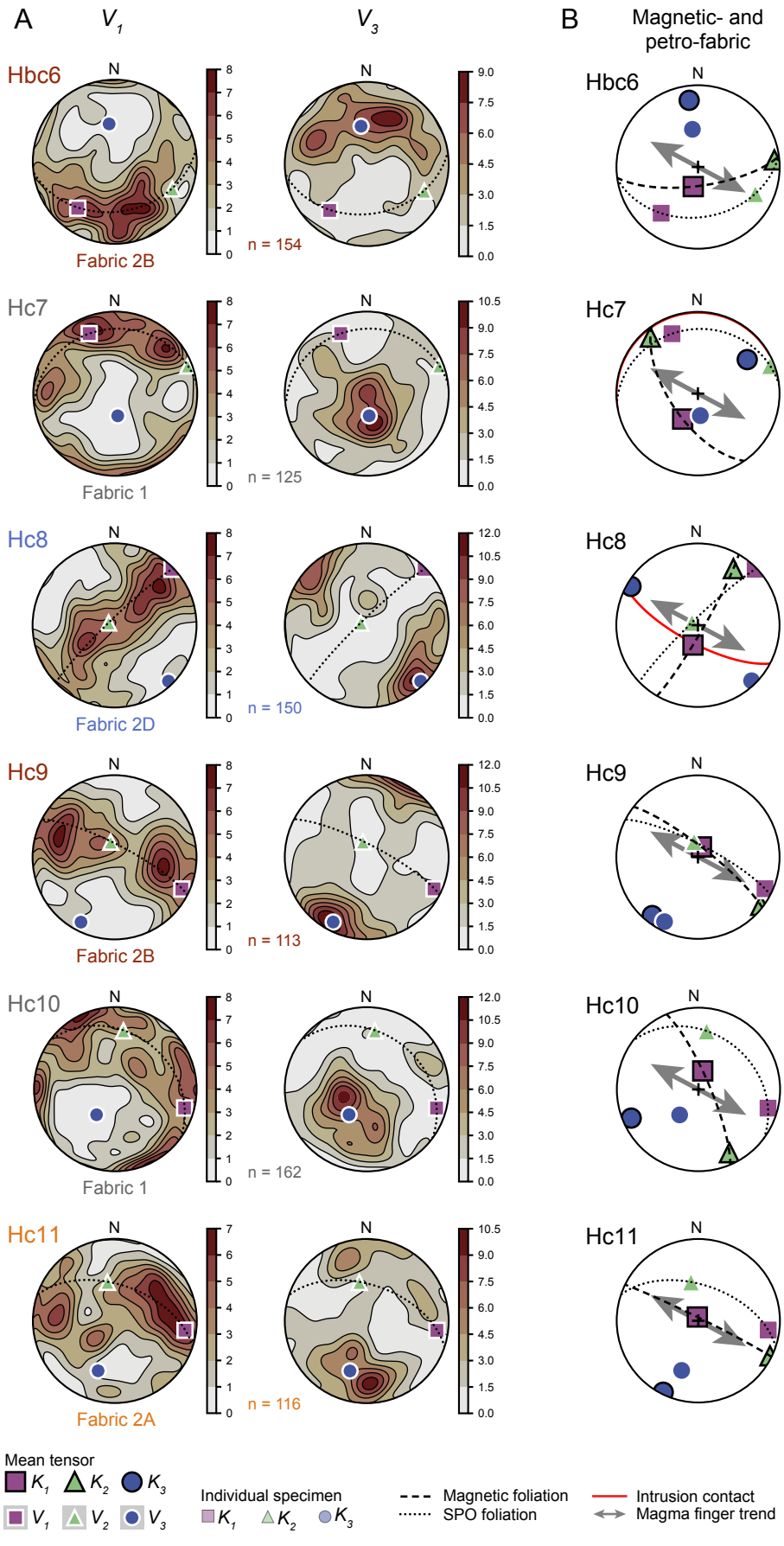
A
V_1
V_3
B
Magnetic- and petro-fabric
Hbc6
N
n = 154
Fabric 2B
Hc7
n = 125
Fabric 1
Hc8
n = 150
Fabric 2D
Hc9
n = 113
Fabric 2B
Hc10
n = 162
Fabric 1
Hc11
n = 116
Fabric 2A
Mean tensor
K_1 K_2 K_3
V_1 V_2 V_3
Individual specimen
K_1 K_2 K_3
Magnetic foliation
SPO foliation
Intrusion contact
Magma finger trend

Figure 11: (A) Equal-area, lower hemisphere stereonet plots show the orientation density distribution of long axes (V_1) and short axes (V_3) orientations of clinopyroxene and olivine crystals for one sample in the intrusive step (Hbc6) and for finger Hc (Hc7–Hc11); average petrofabric tensor axes orientations (V_1, V_2, V_3) are indicated. (B) Equal-area, lower hemisphere stereonet plots show the comparison of AMS (K_1, K_2, K_3) and petrofabric tensor (V_1, V_2, V_3) axes orientations.

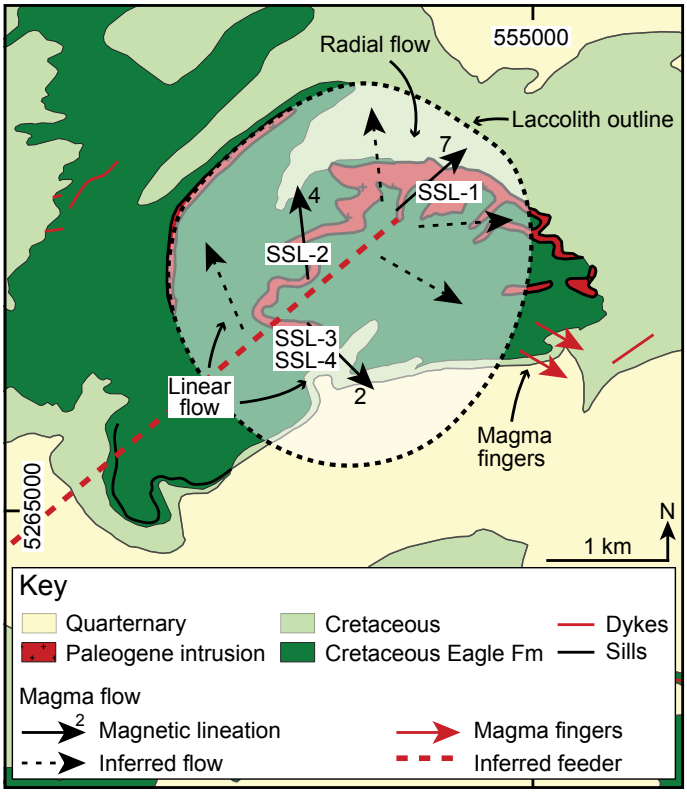

Figure 12: Simplified geological map of the Shonkin Sag laccolith shows the potential feeder-dyke location, magnetic lineation orientations, and inferred magma flow pathways. The plunge of magnetic lineations is indicated at the tip of solid black arrows. The geological map is based on the quadrangle 'Fort Benton' (1:100,000 scale) available from the Montana Bureau of Mines and Geology (2021); laccolith outline after Hurlbut Jr. (1939).

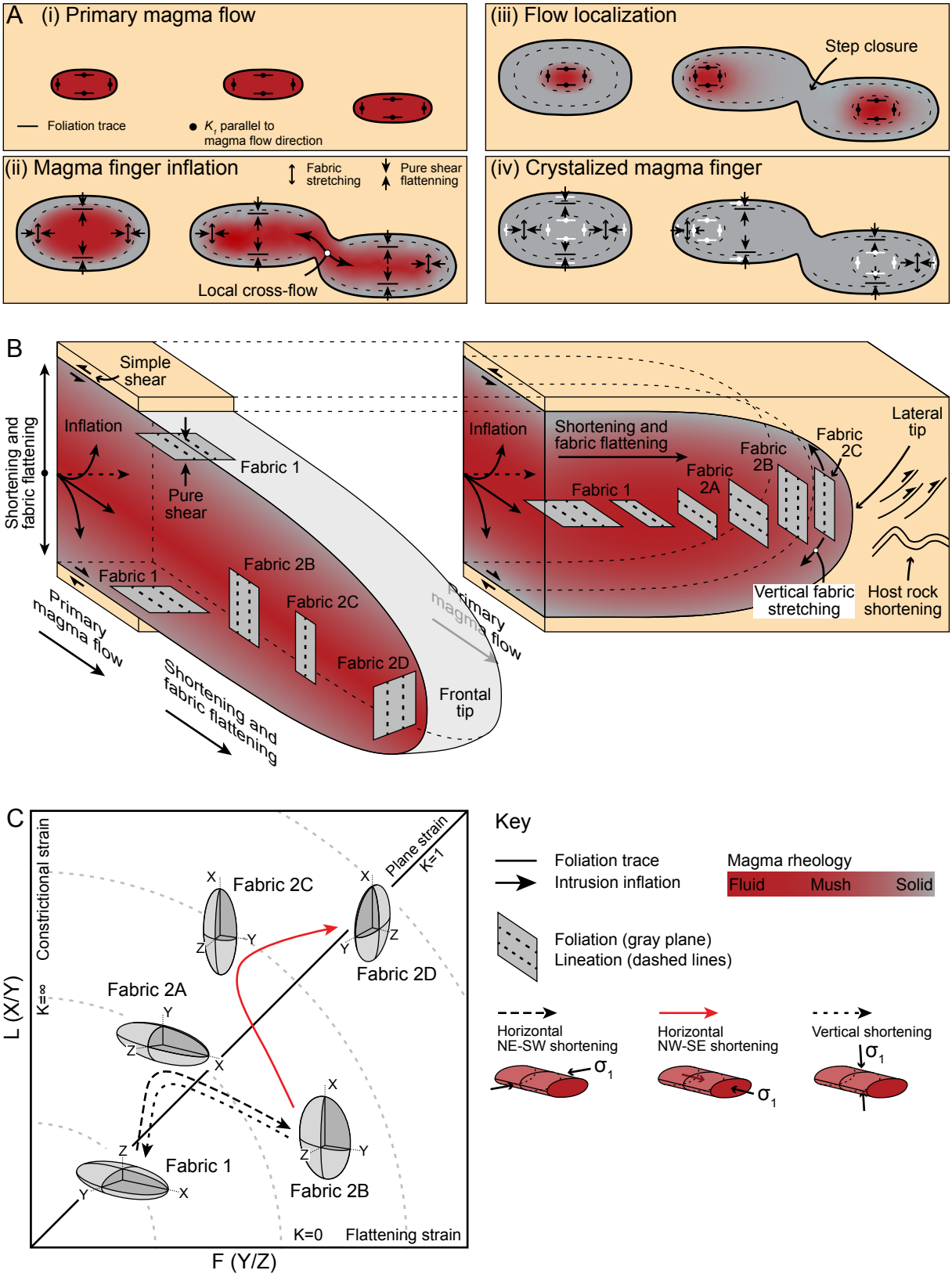

Figure 13: (A) Schematic cross-section diagrams show a time series of mama finger emplacement; cross sections are oriented perpendicular to both the magma finger long axis and the primary magma flow direction. Magma flow and emplacement processes and the expected

associated fabrics are indicated. Note that changing magma flow dynamics and local magma solidification can result in adjacent fabrics that are not directly related (iv). (B) Schematic 3-D diagram shows all fabric types as observed in the magma fingers studied, their spatial occurrence, and how they may develop over time. Magma flow processes such as primary flow, inflation, and fabric stretching/flattening are indicated. (C) Schematic Flinn diagram shows interpreted strain paths and fabric overprinting due to primary magma flow and both horizontal and vertical inflation.

Table 1: *Petrofabric analyses results*

SPO: Cpx and Ol

Sample	n	V_1		V_2		V_3		Foliation			P_j	T	Contact to host rock			α	β	Fabric
		Dec. (º)	Pl. (º)	Dec. (º)	Pl. (º)	Dec. (º)	Pl. (º)	Strike (º)	Dip (º)	Dip dir.			Strike (º)	Dip (º)	Dip dir.	(º)	(º)	
JJ-2	77	073	04	163	04	296	84	026	06	SE	2.657	0.38	138	03	NE	71	62	Fabric 1
Hbc6	154	219	28	115	24	351	52	081	38	S	2.047	0.45	-	-	-	37	79	Fabric 2B
Hc7	125	337	21	069	06	174	68	084	22	N	2.228	0.58	079	01	NNW	34	39	Fabric 1
Hc8	150	046	02	295	83	136	06	046	84	NW	2.669	0.52	118	72	SW	72	72	Fabric 2D
Hc9	113	115	10	346	74	207	12	117	78	NE	3.209	0.39	-	-	-	1	3	Fabric 2B
Hc10	162	105	13	008	29	217	58	127	32	NE	2.603	0.78	-	-	-	9	13	Fabric 1
Hc11	128	098	15	349	50	199	36	109	54	NNE	1.900	-0.10	-	-	-	9	20	Fabric 2A

DA: oxides

Sample	n	λ_1		λ_2		λ_3		Foliation			P_j	T
		Dec. (º)	Pl. (º)	Dec. (º)	Pl. (º)	Dec. (º)	Pl. (º)	Strike (º)	Dip (º)	Dip dir.		
JJ-2	8746	036	18	300	16	171	66	081	24	N	1.112	-0.63
Hbc6	2271	051	36	222	54	318	04	048	86	SE	1.122	0.04
Hc7	2660	158	68	039	11	305	19	035	71	SE	1.151	-0.27
Hc8	8980	312	88	049	00	139	02	049	88	NW	1.034	0.22
Hc9	4241	300	02	046	81	209	09	119	81	NE	1.089	-0.06
Hc10	2843	015	15	107	06	218	73	128	17	NE	1.124	-0.04
Hc11	364	041	47	164	27	272	31	002	59	E	1.240	0.06

Note: SPO–shape preferred orientation; DA–distribution anisotropy; n–number of analyzed grains; Dec.–declination; Pl.–plunge; Dip dir.–dip direction; P_j–corrected degree of anisotropy; T–shape parameter. Measurements are collected from one representative specimen of each sample.

Table 2: *Anisotropy of magnetic susceptibility results*

ip-AMS

Group & Sample ID	n	K_1		K_2		K_3		Magnetic foliation			K_m	P_j	T	Contact to host rock			α	β	Fabric
		Dec. (º)	Pl. (º)	Dec. (º)	Pl. (º)	Dec. (º)	Pl. (º)	Strike (º)	Dip (º)	Dip dir.	10^{-2} SI			Strike (º)	Dip (º)	Dip dir.	(º)	(º)	
SSL-01	88	229	07	139	03	026	82	116	08	SSW	2.78	1.016	0.25	-	-	-	-	-	Fabric 1
SSL-02	94	173	04	263	02	019	86	109	04	SSW	4.31	1.023	0.39	-	-	-	-	-	Fabric 1
SSL-03	20	309	01	219	02	065	87	155	03	SW	3.86	1.023	0.52	-	-	-	-	-	Fabric 1
SSL-04	60	314	02	224	14	052	75	142	15	SW	2.84	1.014	0.34	-	-	-	-	-	Fabric 1
II-1	6	142	72	325	18	235	01	145	89	NE	3.63	1.029	0.35	145	80	SW	0	3	Fabric 2B
II-2	6	342	39	192	47	085	16	175	74	WSW	4.10	1.019	-0.49	114	01	NE	30	17	Fabric 2A
II-3	6	157	81	023	06	292	06	022	84	E	3.68	1.027	0.20	-	-	-	57	12	Fabric 2D
II-4	6	350	09	090	48	253	41	163	49	E	3.03	1.030	-0.31	121	02	NE	18	25	Fabric 2A
II-5	6	316	28	191	47	063	30	153	60	SW	3.73	1.018	-0.16	-	-	-	8	9	Fabric 2A
JJ-1	7	207	12	080	70	300	15	030	75	SE	3.32	1.025	-0.11	-	-	-	75	72	Fabric 2D
JJ-2	6	327	03	057	02	176	86	086	04	N	3.80	1.012	-0.06	138	03	NE	49	12	Fabric 1
JJ-3	6	133	05	026	72	225	17	135	73	NE	4.30	1.020	-0.21	-	-	-	0	2	Fabric 2A
JJ-4	7	117	03	207	05	356	85	086	05	S	0.04	1.011	0.39	126	02	NE	49	18	Fabric 1
JJ-5	6	248	83	131	03	041	07	131	83	SW	1.94	1.027	0.13	135	80	NE	4	67	Fabric 2B
Hb1	5	050	20	148	22	283	60	013	30	E	2.76	1.024	0.08	104	02	NNE	75	68	Fabric 1
Hb2	5	129	37	342	48	233	17	143	73	NE	3.87	1.010	-0.45	-	-	-	25	11	Fabric 2A
Hb3	6	251	18	156	16	027	65	117	25	SW	3.06	1.015	-0.41	108	02	NNE	1	47	Fabric 1
Hb4	5	261	85	033	04	124	04	034	86	NW	3.54	1.021	0.05	-	-	-	84	37	Fabric 2D
Hbc5	4	162	51	044	21	301	32	031	58	SE	2.35	1.014	-0.15	143	18	NE	87	44	Fabric 2D
Hbc6	6	194	70	085	07	352	19	082	71	S	2.23	1.015	0.41	-	-	-	36	76	Fabric 2B
Hc7	5	211	60	320	11	055	27	145	63	SW	2.78	1.014	0.44	079	01	NNW	27	87	Fabric 2B
Hc8	8	194	70	032	19	300	06	030	84	SE	2.88	1.025	0.03	118	72	SW	88	76	Fabric 2D
Hc9	8	019	79	127	03	218	10	128	80	NE	2.10	1.022	0.20	-	-	-	10	81	Fabric 2B
Hc10	5	013	71	154	15	247	11	157	79	NE	2.65	1.016	-0.31	-	-	-	39	75	Fabric 2C
Hc11	8	345	86	116	03	206	03	116	87	NE	2.51	1.015	-0.25	-	-	-	2	47	Fabric 2C

Note: AMS–anisotropy of magnetic susceptibility; n–number of analyzed specimens; Dec.–declination; Pl.–plunge; Dip dir.–dip direction; K_m–average magnetic susceptibility; P_j–corrected degree of anisotropy; T–shape parameter. Presented measurements are group/sample mean data.